

1   **Controls on sinking velocities and mass fluxes of size-fractionated marine**  
2   **particles in recent U.S. GEOTRACES cruises**

3  
4   Yang Xiang<sup>1,\*</sup>, Phoebe J. Lam<sup>1</sup>, Adrian B. Burd<sup>2</sup>

5  
6   <sup>1</sup>Department of Ocean Sciences, University of California, Santa Cruz, CA 95064 USA

7   <sup>2</sup>Department of Marine Sciences, University of Georgia, Athens, GA 30602 USA

8  
9   \*Corresponding author: Yang Xiang, E: [yaxiang@ucsc.edu](mailto:yaxiang@ucsc.edu), P: 1-831-212-5119

10   University of California Santa Cruz, 1156 High Street, Santa Cruz, CA 95064

11  
12   Key Points:

- 13   - Incorporation of ballast minerals into natural marine aggregates away from the sediment
- 14   resuspension is likely not to alter particle size;
- 15   - The effect of size on total mass flux is often not as important as particle composition, due
- 16   to particle mass partitioning and porosity;
- 17   - The western Arctic Ocean is characterized by lowest total mass flux due to its small sizes,
- 18   low particle concentrations and viscous water.

19

20

21

22

23

24

25

26

27

28

29

30

31

32

33

34

35

36

37

38

39

40

41

42

43

44

45

46

47     **Abstract**  
48         Particle composition is an important parameter that influences sinking velocity of marine  
49         particles. Most current studies, however, are limited by either a lack of routine measurements of  
50         particle composition or low sampling resolution in the water column. Here, we compile full ocean-  
51         depth size-fractionated (1-51 and >51  $\mu\text{m}$ ) particle concentration and composition of suspended  
52         particulate matter from three recent U.S. GEOTRACES cruises to calculate their corresponding  
53         sinking velocity and mass flux. Our model is based on Stokes' Law and incorporates a newly  
54         updated power-law relationship between particle size and porosity. The integration of the porosity-  
55         size relationship decreases the power applied to size in Stokes' Law to 0.8. The medians of average  
56         sinking velocity in total particles are 15.4, 15.2, and 7.4 m/d, in the North Atlantic, Southeast  
57         Pacific, and western Arctic Ocean, respectively. We examine the relative importance of particle  
58         concentration, composition, size, and hydrography on sinking fluxes. Particle concentration is the  
59         major control of the variability and magnitude of mass flux, while particle composition is the  
60         second most important term. Increasing porosity with aggregate size and a dominance of smaller  
61         particles diminishes the importance of the size dependence in mass flux, elevating the relative  
62         importance of composition and thus density. Viscosity of seawater can result in up to a factor of  
63         two difference in mass flux between polar and tropical oceans. This work serves as one of the first  
64         studies to offer quantitative perspectives for the contribution from different factors to mass flux in  
65         field observations of marine particles.

66  
67     **Plain language summary**  
68         In this study, we compile concentrations and chemical compositions of marine suspended  
69         particles from the surface to seafloor on a global scale, and evaluate potential factors controlling  
70         the particle sinking flux. Estimating how fast particles sink and the magnitude of particle flux can  
71         help us better understand the global carbon budget. Our results demonstrate the primary  
72         importance of particle concentration affecting the particle flux. For example, at places with higher  
73         biological production and thereby higher particle concentrations, samples collected are  
74         characterized by increased particle flux. Other factors, such as the chemical composition and size  
75         of marine particles and viscosity of seawater compete for influence: some mineral phases in  
76         particles, characterized by higher densities, potentially offer excess weights to enhance the particle  
77         flux; smaller particles tend to sink slower compared to larger particles because of their sizes. In  
78         the high-latitude Arctic Ocean, marine particles have high concentrations of ballasting minerals,  
79         however, this alone cannot outcompete the most viscous water, smallest particle size and  
80         concentrations, leading to much smaller mass fluxes compared to tropical oceans.

81  
82         Keywords: Sinking velocity, Total mass flux, Porosity, Ballast effect, Biological pump,  
83         GEOTRACES

84  
85  
86  
87  
88  
89  
90  
91  
92

93     **1. Introduction**

94       The marine biological carbon pump (BCP) plays a crucial role in the global carbon cycle  
95 by fixing carbon dioxide ( $\text{CO}_2$ ) in the surface water into particulate organic matter (POM), which  
96 then sinks into the deep ocean (Kwon et al., 2009; Volk & Hoffert, 1985). Particle dynamics in the  
97 water column, including particle remineralization, aggregation, and disaggregation, are of  
98 significance in modifying and attenuating POM during sinking (Lam & Marchal, 2015). Most of  
99 the sinking flux is composed of phytoplankton aggregates, marine snow, and fecal pellets (Alldredge  
100 & Silver, 1988; Bishop et al., 1977; Ebersbach & Trull, 2008; Fowler & Knauer, 1986;  
101 Laurenceau-Cornec et al., 2015a; Turner, 2015; Wilson et al., 2013). Only a small fraction of POM  
102 (~10%) produced at the surface, however, sinks below mesopelagic regions (Martin et al., 1987).

103       Conceptually, vertical mass flux is calculated as the product of the sinking velocity and  
104 particle concentration. It is closely related to particle properties, such as concentration, size, and  
105 composition. While particle flux should scale with concentration, this is modulated by variations  
106 in sinking speed caused by differences in particle size, shape, and excess density. Numerous  
107 studies measure POC fluxes using sediment traps (e.g., Buesseler et al., 2007), and POC  
108 concentrations using large-volume filtration (e.g., Bishop et al., 1977; Lam et al., 2011). Variations  
109 in the relationship between flux and concentration reflect the variation in sinking speed. The  
110 importance of particle size on carbon export is apparent from Stokes' Law (Stokes, 1851), which  
111 shows that the sinking velocity is proportional to the square of particle diameter. Despite only  
112 holding for spherical solid particles at low Reynolds number, Stokes' Law has been widely used  
113 to characterize the sinking speed of marine particles (e.g., Laurenceau-Cornec et al., 2020;  
114 McDonnell & Buesseler, 2010; Omand et al., 2020), giving insights into the complicated system  
115 of the BCP. Similar to particle size, particle composition is also known to affect the export flux  
116 via its relationship with sinking velocity. The existence of mineral ballast, such as  $\text{CaCO}_3$  and  
117 lithogenic particles, has been suggested to provide a source of excess density and/or protection and  
118 promote carbon export into the deep ocean (Armstrong et al., 2001; Francois et al., 2002; Klaas &  
119 Archer, 2002). Opal is a less efficient ballast mineral as a result of its lower density and/or higher  
120 porosity (Bach et al., 2016; Francois et al., 2002; Iversen & Ploug, 2010; Lam & Bishop, 2007;  
121 Lam et al., 2011; Puigcorbé et al., 2015). The ballast effect, however, is still under active debate  
122 (Aumont et al., 2017; Boyd & Trull, 2007; Henson et al., 2012; Lam & Bishop, 2007; Le Moigne  
123 et al., 2012; Lee et al., 2009; Rosengard et al., 2015), since indirect ecosystem effects are difficult  
124 to disentangle from direct effects of mineral density (e.g., Lima et al., 2014).

125       Thanks to the GEOTRACES program, measurements of particle concentration and  
126 composition in the North Atlantic, equatorial Southeast Pacific, and western Arctic Ocean have  
127 been made in the past decade, covering many different geographic regions (Lam et al., 2018; Lam  
128 et al., 2015; Xiang & Lam, 2020). The three ocean basins are characterized by different sources of  
129 particles, therefore different particle compositions. This study utilizes the composition data from  
130 these recent U.S. GEOTRACES cruises and applies mass-size and porosity-size power-law  
131 functions to calculate the corresponding size-fractionated sinking velocity and mass flux. Despite  
132 lacking the seasonal resolution, this data offers higher spatial and depth resolution of sinking  
133 particle fluxes than existing sediment traps, and allows us to investigate the relative importance of  
134 particle concentration, composition (density), particle size, and hydrography on particle sinking  
135 fluxes. Indeed, the model used here can be adapted to any other size-fractionated particulate phases  
136 and trace metals to calculate their corresponding mass fluxes, given the assumption that the  
137 specific particulate phase has the same sinking rate as the bulk particles. Insights gained in this  
138 study help us understand the role of particle characteristics on carbon flux, which can be applied

139 to other regions in future studies to improve our understanding of the biological pump on a global  
140 scale. It is particularly important, for most model projections suggest a decline in the carbon export  
141 to the deep ocean under the current warming scenario (Bopp et al., 2013; Cavan et al., 2019;  
142 Laufkötter et al., 2016).

143

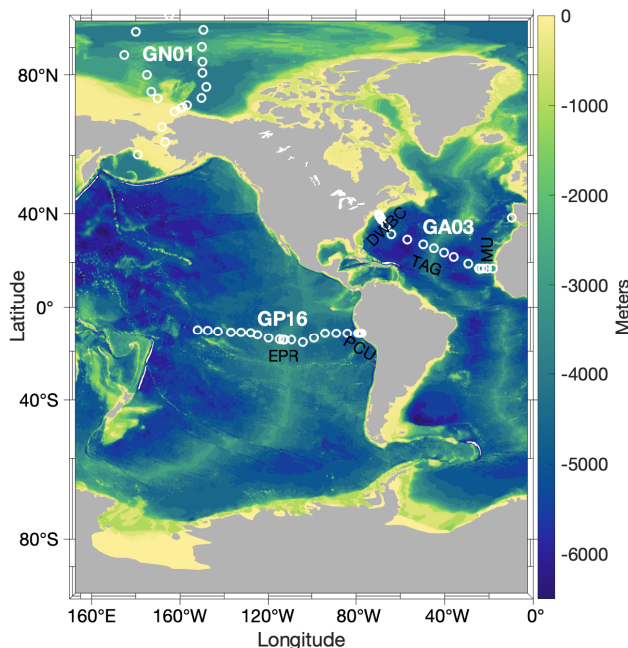
## 144 **2. Materials and Methods**

### 145 2.1 Cruise tracks and sampling method

146 The U.S. GEOTRACES North Atlantic Zonal Transect (GA03) cruise, was completed with  
147 two legs in 2010-2011 in the subtropical North Atlantic (Figure 1). The cruise track sampled the  
148 Mauritanian Upwelling system, the North Atlantic deep western boundary current, and the Trans-  
149 Atlantic Geotraverse (TAG) hydrothermal plume on the slowly-spreading Mid-Atlantic Ridge.  
150 The Eastern Pacific Zonal Transect (GP16) cruise was completed in the Southeast (SE) Pacific  
151 Ocean in October–December 2013 (Figure 1). The expedition sampled the Peruvian Coastal  
152 upwelling region, the oxygen deficient zone (ODZ) off Peru, and the superfast-spreading East  
153 Pacific Rise (EPR) hydrothermal plume. The U.S. Arctic cruise (GN01) focused on the western  
154 Arctic Ocean and sampled at both very productive shallow shelves and extremely oligotrophic  
155 deep basins in 2015 (Figure 1). The Arctic Ocean is characterized by extremely broad continental  
156 shelves, consisting of 53% of its overall area (Jakobsson, 2002).

157 Size-fractionated particles were all sampled using dual-flow McLane Research in-situ  
158 pumps (WTS-LV). Large size fraction particles are referred to as “LSF”, representing the size  
159 fraction of  $>51\text{ }\mu\text{m}$ , whereas the small size fraction, “SSF”, are particles between 1 and  $51\text{ }\mu\text{m}$ .  
160 Total particles are defined as the sum of both size fractions (Total= LSF+SSF). More details about  
161 the cruise hydrography, sample handling and analytical methods of different particle compositions  
162 can be found in Lam et al. (2015), Lam et al. (2018), Xiang and Lam (2020).

163



164

165 Figure 1. Station map of three U.S. GEOTRACES cruises in which in-situ pump were deployed.  
166 The color bar is ocean bathymetry (using *haline* in cmocean colormap) (Thyng et al., 2016). The  
167 GA03 is the North Atlantic Zonal Transect, GP16 is the Eastern Pacific Zonal Transect, and GN01

168 is the Arctic cruise. MU: Mauritanian Upwelling; TAG: Trans-Atlantic Geotraverse hydrothermal  
169 plume; DWBC: deep western boundary current; PCU: Peruvian Coastal Upwelling; EPR: East  
170 Pacific Rise (EPR) hydrothermal plume.

## 172 2.2 Porosity and size relationship

173 The porosity is defined as the volume fraction of an aggregate that is not occupied by solid  
174 matter and tends to increase with particle size (Alldredge & Gotschalk, 1988). It is an essential  
175 parameter in the calculation of particle volume and mass flux from size (Jackson et al., 1997;  
176 Stemmann et al., 2008). Alldredge and Gotschalk (1988) pioneered porosity measurements in  
177 marine aggregates and found a power-law relationship between the porosity and particle size by  
178 direct measurements in situ:

$$1-P_i = (8 \times 10^{-3}) \times (d_i/10^3)^{-1.6} \quad (1)$$

179 where  $P_i$  is the particle porosity for size bin  $i$  and is unitless,  $d_i$  is the equivalent spherical diameter  
180 of particles ( $\mu\text{m}$ ), and  $10^3$  is the conversion factor between  $\mu\text{m}$  and mm. This classic power  
181 function was used to calculate the particle sinking velocities in many studies (e.g., Burd et al.,  
182 2007; Ruiz, 1997). Data points from Alldredge and Gotschalk (1988) were extracted using  
183 WebPlotDigitizer (Rohatgi, 2010) for this study. The extracted regression equation is  
184  $1-P_i = (8.2 \times 10^{-3}) \times (d_i/10^3)^{-1.6}$ , which is similar to the original one.

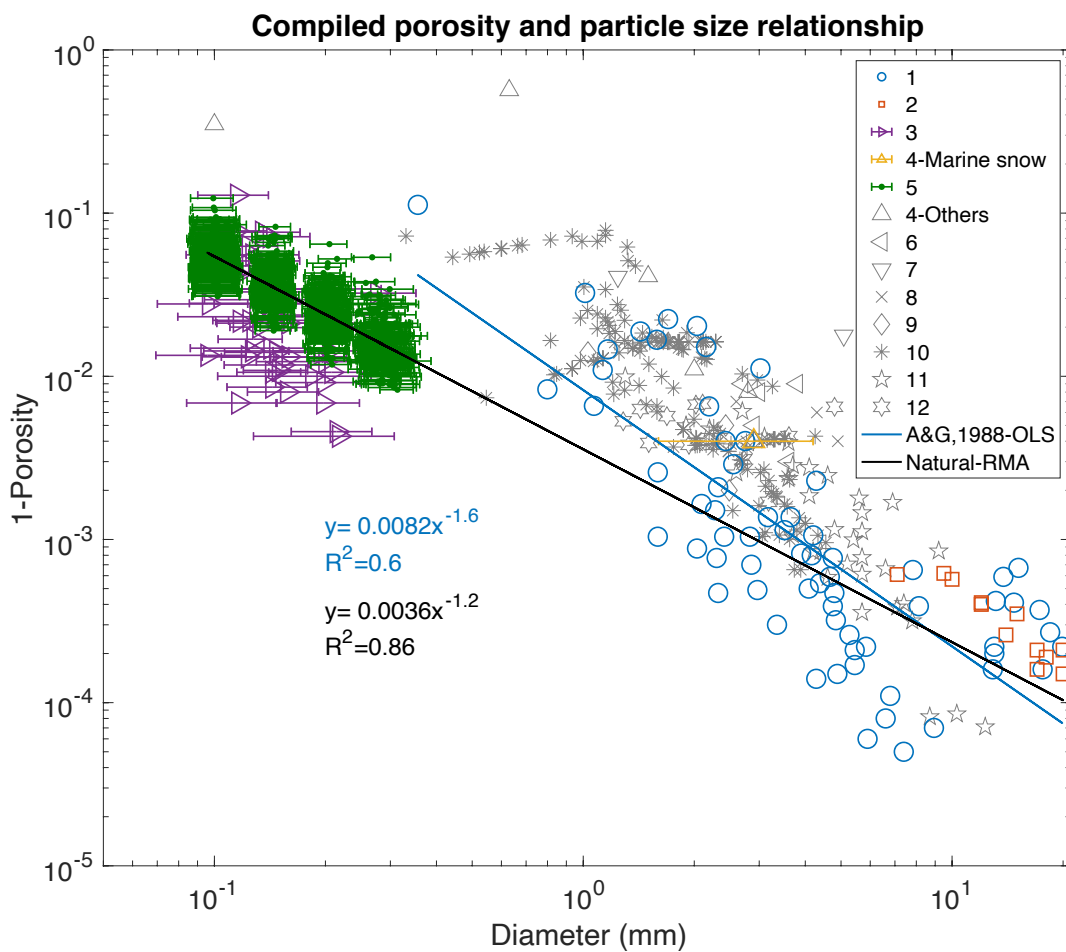
185 In the past 30 years, there have been several additional studies measuring porosity and size  
186 of marine aggregates (Figure 2) (Bach et al., 2016; Engel et al., 2009; Iversen & Robert, 2015;  
187 Lam & Bishop, 2007; Laurenceau-Cornec et al., 2020; Laurenceau-Cornec et al., 2015b; Logan &  
188 Alldredge, 1989; Ploug et al., 2008a; Ploug & Passow, 2007; Prairie et al., 2015; Schmidt et al.,  
189 2014). A detailed summary of all data sources and analytical methods is listed in Table S1. Due to  
190 the difficulties of measuring size and porosity in situ in the water column, many of these studies  
191 were conducted with aggregates formed in lab roller tanks, while others measured bulk properties  
192 from which we estimated particle size distributions. For example, the Lam and Bishop (2007)  
193 study estimated porosities of bulk size-fractionated ( $1-51 \mu\text{m}$  and  $>51 \mu\text{m}$ ) particles collected by  
194 in-situ filtration in the Southern Ocean. To estimate a mean particle size for each size fraction to  
195 associate with estimated porosities, we used nearby particle size distributions obtained by the  
196 Underwater Vision Profiler (UVP) in the Lohafex 2009 and Tara 2011 cruises in the Subantarctic  
197 and Antarctic, respectively (Picheral et al., 2017). It is noted that natural aggregates are different  
198 from aggregates formed in roller tanks and characterized by smaller sizes (Laurenceau-Cornec et  
199 al., 2015b). Further, for a given size, it also seems that natural aggregates have a higher porosity  
200 (lower  $(1-P_i)$ ) than similarly-sized lab formed aggregates (Figure 2). Since marine particles are all  
201 collected in situ in our dataset, we only use natural marine particles in our updated regression.

202 Compared to Eq. 1, we also used a different linear regression model. The ordinary least  
203 square (OLS) regression used in Alldredge and Gotschalk (1988) is sensitive to changes in X-axis  
204 scale (i.e., meter vs. millimeter). Therefore, a Model-II reduced major axis (RMA) regression was  
205 used, as implemented in lsqfitgm.m in MATLAB by E.T. Peltzer (<https://www.mbari.org/index-of-downloadable-files/>). The updated power-law relationship between (1-porosity) and particle  
206 sizes is:

$$1-P_i = (3.6 \times 10^{-3}) \times (d_i/10^3)^{-1.2} \quad (2)$$

208 Compared to the original Alldredge and Gotschalk (1988) relationship (Eq. 1), this new  
209 relationship has a weaker dependency of porosity with size, but also has a lower coefficient. Logan  
210 and Wilkinson (1990) illustrated the relationship between the fractal dimension  $D_3$  and the power

211 exponent b in the porosity-size function, where  $D_3=3+b$ . The value of the fractal dimension depicts  
 212 how much space the solid occupies in three dimensions. A pure solid has a fractal dimension of 3.  
 213 The fractal dimensions in our updated and original Alldredge and Gotschalk (1988) relationship  
 214 are 1.8 and 1.4, respectively, which means that marine particles in this study are more compact  
 215 than those in Alldredge and Gotschalk (1988). Despite the higher fractal dimension in our new  
 216 relationship, the coefficient is lower, resulting in higher porosities over the size range of most  
 217 marine particles (Figure 2). The intersection between the original Eq. 1 and new Eq. 2 occurs at  
 218 8.3 mm; therefore, particles smaller than 8.3 mm have a higher porosity (lower  $1-P_i$ ) in the newly  
 219 compiled porosity-size relationship (Figure 2). Additionally, the new relationship predicts a  
 220 particle size of about 8.6  $\mu\text{m}$  when the porosity approaches 0, compared to 48.9  $\mu\text{m}$  for the original  
 221 Alldredge and Gotschalk (1988) relationship. We treat particles as pure solids ( $P_i=0$ ) for all sizes  
 222 below 8.6  $\mu\text{m}$ .



223  
 224 Figure 2. The newly compiled porosity-size relationship from literature. Data points outlined in  
 225 gray are aggregates formed in lab roller tanks, whereas colored symbols are natural marine  
 226 aggregates. The ordinary least square (OLS) and reduced major axis (RMA) regression are used  
 227 to fit data from Alldredge and Gotschalk (1988) and all natural aggregates, respectively.  
 228 Regression equations are displayed with the colors matching with fit lines. 1: Alldredge and  
 229 Gotschalk (1988); 2: Logan and Alldredge (1989); 3: Lam and Bishop (2007); 4: Ploug et al.  
 230 (2008a); 5: Bach et al. (2016); 6: Ploug and Passow (2007); 7: Engel et al. (2009); 8: Schmidt et

231 al. (2014); 9: Prairie et al. (2015); 10: Iversen and Robert (2015); 11: Laurenceau-Cornec et al.  
 232 (2015b); 12: Laurenceau-Cornec et al. (2020).

### 234 2.3 Particle sinking rate calculation

235 Stokes' Law has been widely used to calculate sinking velocities of marine particles  
 236 (Stokes, 1851). In this simple model assuming spherical particles, laminar flow, and a smooth  
 237 surface, the sinking velocity increases with particle size and excess density, the density difference  
 238 between solid materials and seawater:

$$W_i = \frac{g\Delta\varrho(d_i/10^6)^2}{18\eta} \quad (3)$$

239 where  $W_i$  is the sinking velocity for size bin  $i$  with the unit of m/s,  $g$  is the gravitational  
 240 acceleration in m/s<sup>2</sup>,  $\Delta\varrho$  is the excess density in kg/m<sup>3</sup>,  $10^6$  is the conversion factor between µm  
 241 and m, and  $\eta$  is the dynamic viscosity of seawater in kg/m/s. Considering porosity, and assuming  
 242 that flow through the porous aggregate is negligible (although see section 4.4), Eq. 3 becomes:

$$W_i = (1-P_i) \frac{g\Delta\varrho(d_i/10^6)^2}{18\eta} \quad (4)$$

243 Combing Eqs. 2 and 4 explicitly and using m as the unit for particle size, the sinking  
 244 velocity is calculated as:

$$W_i = (3.6 \times 10^{-11.4}) \times \frac{g\Delta\varrho(d_i)^{0.8}}{18\eta} \quad (5)$$

245 Since  $1-P_i$  decreases (porosity increases) with particle size (Eqs. 1-2), sinking velocities in  
 246 Eqs. 4-5 have a weaker dependence on the particle size compared to the original Stokes' Law (Eq.  
 247 3). As a result, the influence of other parameters, such as the excess density and viscosity, becomes  
 248 more important. It is also worth noting that a slightly stronger size dependency in sinking velocity  
 249 occurs with the implementation of the newly compiled porosity and size relationship (Eq. 2) to Eq.  
 250 5 when compared to using the original relationship from Alldredge and Gotschalk (1988) (Eq. 1).

251 The Stokes' Law is only valid at low Reynolds number ( $Re$ ) in the laminar flow regime,  
 252 empirically found at  $Re < 0.5$  (White, 1974). The Reynolds number is:

$$Re = \frac{\varrho_{sw} W(d_i/10^6)}{\eta} \quad (6)$$

253 where  $\varrho_{sw}$  is the density of seawater (unit: kg/m<sup>3</sup>). With the consideration of increasing porosity  
 254 with size, however, Stokes' Law is potentially valid at higher Reynolds numbers ( $1 < Re < 50$ )  
 255 (Laurenceau-Cornec et al., 2020). Indeed, roller-tank aggregates with minerals were best modelled  
 256 using Stokes' Law with constant porosity (99%), and also well described with a form of Stokes'  
 257 Law modified with a fractal-porosity relationship (Laurenceau-Cornec et al., 2020), similar to our  
 258 Eq. 5. However, for aggregates without minerals, the modified Stokes' law with the fractal-  
 259 porosity relationship modelled the sinking velocity much better than using constant porosity. Even  
 260 though the observation was not based on naturally formed marine aggregates, it is still our best  
 261 understanding of the applicability of Stokes' Law to marine particles, and we use Eq. 5 to estimate  
 262 sinking velocities of our natural mineral-containing particles. It is noteworthy that the fractal-  
 263 porosity relationship for natural marine aggregates used in this study (Eq. 2) has a lower coefficient  
 264 but similar fractal dimension compared to artificial aggregates in Laurenceau-Cornec et al. (2020).  
 265 Lower coefficients can be visualized with Figure 2, where natural aggregates seem to have a lower  
 266 intercept than roller tanks aggregates.

267  
268 2.3.1 Particle density calculation

269 Major phases in marine particles include particulate organic matter (POM), opal, lithogenic  
 270 materials (Litho), calcium carbonate ( $\text{CaCO}_3$ ), manganese oxides ( $\text{MnO}_2$ ), and iron oxyhydroxides  
 271 ( $\text{Fe(OH)}_3$ ). The contribution of each particle phase to the overall particle mass, known as the  
 272 compositional fraction, is calculated by normalizing its concentration with suspended particulate  
 273 mass (SPM). Compositional fractions in the LSF and SSF are calculated separately and used in the  
 274 calculations of particle density. The density of the solid portion of particles,  $\rho_{\text{particle}}$ , is calculated  
 275 as:

$$\rho_{\text{particle}} = \rho_{\text{POM}} f_{\text{POM}} + \rho_{\text{opal}} f_{\text{opal}} + \rho_{\text{Litho}} f_{\text{Litho}} + \rho_{\text{CaCO}_3} f_{\text{CaCO}_3} + \rho_{\text{MnO}_2} f_{\text{MnO}_2} + \rho_{\text{Fe(OH)}_3} f_{\text{Fe(OH)}_3} \quad (7)$$

276 where  $\rho_{\text{POM}}$ ,  $\rho_{\text{opal}}$ ,  $\rho_{\text{Litho}}$ ,  $\rho_{\text{CaCO}_3}$ ,  $\rho_{\text{MnO}_2}$ ,  $\rho_{\text{Fe(OH)}_3}$  are the densities of each particle phase, and  $f_{\text{POM}}$ ,  
 277  $f_{\text{opal}}$ ,  $f_{\text{Litho}}$ ,  $f_{\text{CaCO}_3}$ ,  $f_{\text{MnO}_2}$ ,  $f_{\text{Fe(OH)}_3}$  are the compositional fractions (by weight) of each particle phase.  
 278 We use a density of POM  $\rho_{\text{POM}}$  of  $1.05 \text{ g/cm}^3$  (Young, 1994),  $\rho_{\text{opal}}$  of  $2.0 \text{ g/cm}^3$  (Hurd & Theyer,  
 279 1977),  $\rho_{\text{Litho}}$  of  $2.70 \text{ g/cm}^3$  (Rixen et al., 2019),  $\rho_{\text{CaCO}_3}$  of  $2.71 \text{ g/cm}^3$ ,  $\rho_{\text{MnO}_2}$  of  $3.0 \text{ g/cm}^3$ , and  
 280  $\rho_{\text{Fe(OH)}_3}$  of  $3.96 \text{ g/cm}^3$  (Towe & Bradley, 1967).

281  
282 2.3.2 Hydrography

283 Hydrographic data, such as temperature, salinity, dissolved oxygen, and nutrients, were  
 284 measured in each cruise (Cutter et al., 2019; Schlitzer et al., 2018). The potential density  
 285 was calculated using the seawater toolbox version 3.3.1 in MATLAB (MathWorks  
 286 Inc.). Temperature, salinity, and pressure from the bottle data were interpolated linearly to pump  
 287 depths. The seawater density is a function of temperature, salinity, and pressure, and  
 288 the gravitational acceleration was derived from latitude and depth. The seawater viscosity was  
 289 calculated from temperature and salinity based on the equation in Millero (1974).

290  
291 2.3.3 Data binning

292 Both SSF ( $1\text{-}51 \mu\text{m}$ ) and LSF ( $>51 \mu\text{m}$ ) are evenly divided into 25 bins in logarithmic  
 293 space. Since particles of more than 5 mm are generally rare in the ocean (Honjo et al., 1995; Shanks  
 294 & Trent, 1980), we set the upper limit of the LSF to 5 mm. The size range and median for each  
 295 size bin are summarized in Table S2. The center of the bin in log space is used in the calculation  
 296 of sinking speeds and mass fluxes. Since we only have bulk composition information available for  
 297 the SSF and LSF fractions, we assume that all 25 bins in each size fraction have the same particle  
 298 composition, and thereby the same particle densities.

299  
300 2.4 Mass-size spectra

301 A mass-size spectrum is calculated for each sample in all cruises using the measured bulk  
 302 SSF and LSF SPM concentrations. All spectra are assumed to be a power function between  $1 \mu\text{m}$   
 303 and  $5 \text{ mm}$ . LSF and SSF SPM concentrations, together with size boundaries in different size  
 304 fractions, 1, 51 and  $5000 \mu\text{m}$ , were used to constrain the relationships:

$$m_i = pd_i^{-q} \quad (8)$$

$$\text{SPM} = \frac{\int_{d_1}^{d_2} pd_i^{-q} dd}{10^3} \quad (9)$$

305 where  $m_i$  is the dry mass of particles for each bin  $i$  (unit: g/L/m), SPM is the measured dry  
 306 suspended particulate mass in each size fraction (unit: g/m<sup>3</sup>),  $10^3$  is the conversion factor between  
 307  $\mu\text{g}/\text{L}$  and g/m<sup>3</sup>,  $d_1$  is the lower integration boundary, as 1  $\mu\text{m}$  in the SSF or 51  $\mu\text{m}$  in the LSF,  $d_2$   
 308 is the higher integration boundary, as 51 or 5000  $\mu\text{m}$ , and  $p$  and  $q$  are constant parameters that are  
 309 determined from the size-fractionated SPM data for each sample. The coefficient  $q$  is unitless.  
 310

### 311 2.5 Mass flux calculation

312 The mass flux is obtained from the product of SPM concentrations and sinking velocities.  
 313 The mass flux for each size bin,  $F_i$ , is calculated as:

$$314 F_i = \frac{m_i \times W_i}{10^3} \quad (10)$$

315 where  $F_i$  is with the unit of g/m<sup>2</sup>/s/ $\mu\text{m}$ , and  $10^3$  is the conversion factor between  $\mu\text{m}$  and mm. The overall mass flux  $F$  is the sum of mass fluxes in all size bins:

$$316 F = \int_{d_1}^{d_2} \frac{m_i \times W_i}{10^3} dd \quad (11)$$

317 where  $F$  is with the unit of g/m<sup>2</sup>/s. To convert g/m<sup>2</sup>/s to g/m<sup>2</sup>/day, one needs to multiply by 86400 s/day. The SSF and LSF mass flux are calculated separately for each sample. The total mass flux is the sum of SSF and LSF fluxes.

### 320 2.6 Mass-weighted average sinking velocity calculation

321 The calculation of the mass-weighted average sinking velocity for the SSF and LSF size  
 322 fractions uses the mass fraction of each size bin to weight the velocity calculated in each size bin.  
 323 The mass-weighted average sinking velocity WSV (unit: m/s) is computed separately for the SSF  
 324 (1-51  $\mu\text{m}$ ), the LSF (51-5000  $\mu\text{m}$ ), and total particles (1-5000  $\mu\text{m}$ ) as:

$$325 WSV = \frac{\int_{d_1}^{d_2} m_i W_i dd}{\int_{d_1}^{d_2} m_i dd} \quad (12)$$

326 Indeed, the mass flux  $F$  of the SSF, LSF, or total particles is the product of the WSV multiplied by SPM concentrations of the respective size fraction:

$$327 F = WSV \times SPM \quad (13)$$

328 Derived mass flux and WSV in all size fractions (SSF, LSF, and TOT) from three cruises are summarized in Table S3.

### 330 2.7 Statistical Analysis

331 In this paper, two methods of statistical tests are conducted to evaluate whether variables  
 332 in three oceans are significantly different. The choice of the statistical method depends on the  
 333 distribution for given datasets. The normality of data distribution is assessed using the Lilliefors  
 334 test at the 5% significance level. We use the two-sample t-test ( $\alpha=0.05$ ) to examine statistical  
 335 differences between variables if they both have a normal distribution. Otherwise, the Wilcoxon  
 336 rank sum test, known as the Mann-Whitey U test, is used. Most of our derived parameters are not  
 337 normally distributed. Unless otherwise specified, the p value shown is from the Wilcoxon rank  
 338 sum test.

## 339 3. Results

### 340 3.1 Suspended Particulate Mass (SPM)

342 LSF, SSF, and total (TOT) SPM concentrations in three basins tend to decrease with depth  
343 (Figure S1). In general, the SPM is of higher concentrations in the SSF than LSF (see section  
344 3.4.1). The Chukchi Shelf in the western Arctic Ocean has the highest SPM concentrations in all  
345 size fractions, reaching 1.1, 3.2, and 4.0 g/m<sup>3</sup> for the LSF, SSF, and TOT, respectively, approached  
346 only by the bottom nepheloid layer of the western boundary current in the North Atlantic from the  
347 GA03 cruise. In contrast, the Canada Basin of the western Arctic Ocean is characterized by the  
348 lowest SPM concentrations in the LSF ( $p<<0.001$ ). The SSF and TOT SPM concentrations in the  
349 western Arctic Ocean and SE Pacific central basin are not statistically different from each other  
350 ( $p>0.05$ ) but are both significantly smaller than the North Atlantic ( $p<<0.001$ ). Interestingly, most  
351 deviations between the North Atlantic and SE Pacific occur in the deep ocean: there is less SPM  
352 attenuation with depth in the North Atlantic. Inputs from hydrothermal vents are responsible for  
353 the small elevation in SPM concentrations at 2500 m in the EPR 15°S hydrothermal plume in the  
354 SE Pacific. The North Atlantic western boundary has much more prominent bottom nepheloid  
355 layers (BNLs) than the SE Pacific or Arctic, as found by Gardner et al. (2018a), Gardner et al.  
356 (2018b), and Gardner et al. (2018c).

357

### 358 **3.2 Compositional Fraction**

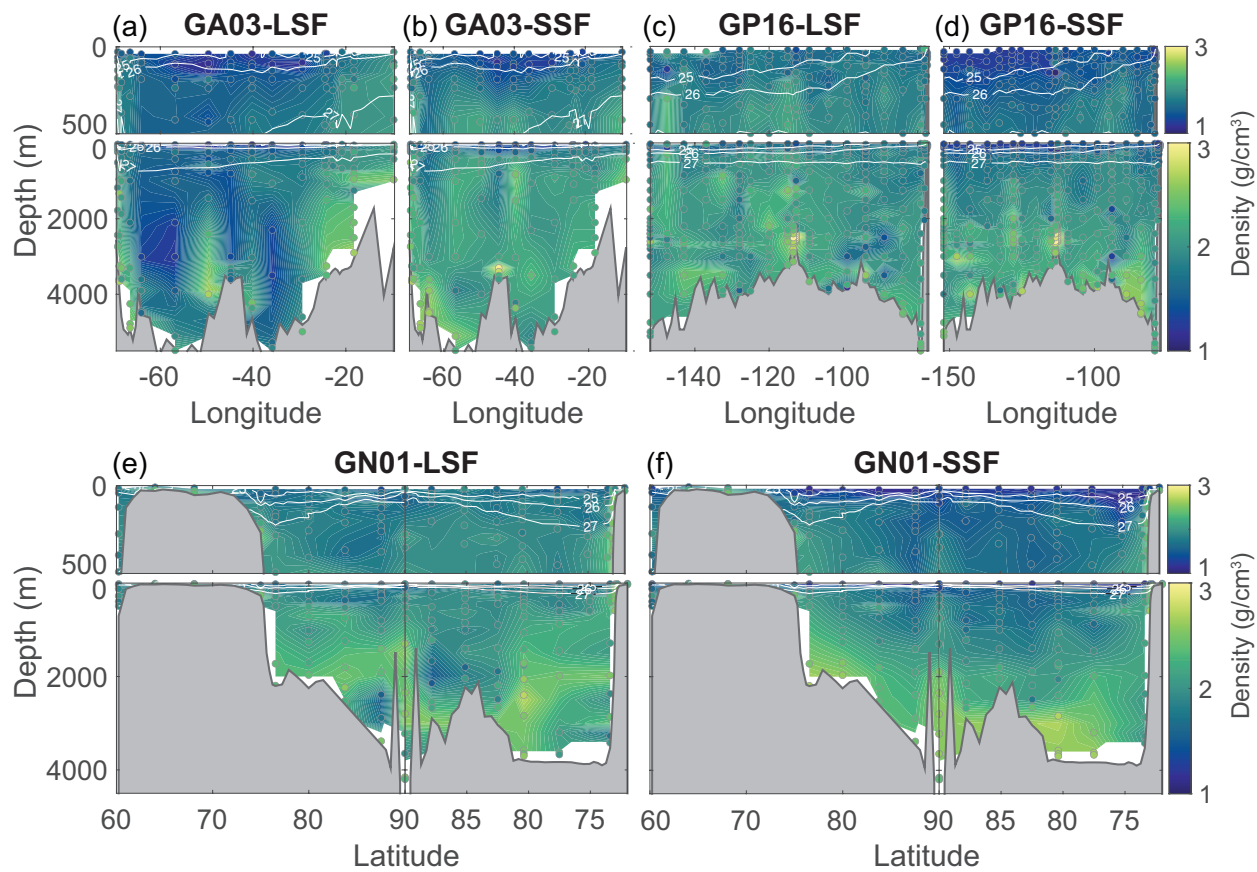
359 The LSF and SSF particles have different particle compositions, with their POM and opal  
360 fractions differing the most. In general, the LSF POM is less dominant than the SSF, whereas the  
361 LSF opal fraction is greater than in the SSF (Figures S2g-j & S3). The POM is the dominant  
362 particle phase in the upper 500 m in both size fractions and the fraction of POM decreases with  
363 depth in all three basins. In contrast, the fraction of lithogenic material progressively increases  
364 with depth (Figures S2e-f & S3). The particulate lithogenic content in the SE Pacific is  
365 significantly smaller than that in the Arctic and North Atlantic ( $p<<0.001$ ). Unlike the North  
366 Atlantic, which is heavily influenced by Saharan dust input (e.g., Mahowald et al., 2005), the  
367 western Arctic Ocean is far from major dust sources, and the supply of lithogenic aerosol particles  
368 into the Arctic Ocean is much smaller (Marsay et al., 2018). The central Arctic Basin receives  
369 most of its lithogenic material via lateral fluxes from the margins (Xiang & Lam, 2020). Prominent  
370 bottom nepheloid layers in the North Atlantic and the western Arctic Ocean are characterized by  
371 high lithogenic fractions, accounting for over 60% of the SPM. CaCO<sub>3</sub>, a biogenic mineral of  
372 similar density to lithogenic particles (see section 2.3.1), is highest in the SE Pacific ( $p<<0.001$ )  
373 and lowest in the Arctic Ocean in both size fractions ( $p<<0.001$ ). The abundance of CaCO<sub>3</sub>  
374 compensates for a lack of lithogenic particles in the SE Pacific, leading to relatively similar  
375 fractions of Litho+CaCO<sub>3</sub> in the three ocean basins (Figure S2c-f). The North Atlantic has the  
376 lowest fraction opal ( $p<<0.001$ ). High opal fractions are observed in the SE Pacific and western  
377 Arctic Ocean, whereas a more definite decreasing trend with depth appears in the western Arctic  
378 Ocean (Figures S2g-h & S3). The Fe(OH)<sub>3</sub> is generally low but elevated in the EPR 15°S and TAG  
379 hydrothermal plumes where the highest fraction of Fe(OH)<sub>3</sub>+MnO<sub>2</sub> consists of up to 60% of SPM  
380 (Figure S2a-b). Despite the absence of hydrothermal activities, the western Arctic Ocean is the  
381 only basin with a relatively high fraction of MnO<sub>2</sub> (>2%) in the entire water column (Figure S3).  
382 The highest fraction in the SSF (~9%) is found in the upper 500 m in the western Arctic Ocean  
383 coinciding with the Pacific-derived halocline, and is even higher than that in the EPR hydrothermal  
384 plume. There is no obvious MnO<sub>2</sub> elevation in the TAG plume, despite similar dissolved  
385 manganese concentrations between the EPR 15°S and TAG plumes (Hatta et al., 2015; Resing et  
386 al., 2015); therefore, the presence of high concentration and fraction of MnO<sub>2</sub> in the EPR 15°S but  
387 not in the TAG (Lam et al., 2018; Lam et al., 2015) is likely a consequence of the comparative

388 ages of the plumes relative to the time scale of dissolved Mn oxidation (Kipp et al., 2018;  
 389 Mandernack & Tebo, 1993).

### 390 3.3 Particle densities and excess densities

392 Particle densities range from 1.1 to 3.2 g/cm<sup>3</sup> in the three sections and generally increase  
 393 with depth (Figure 3). The highest density is found in the EPR 15° S hydrothermal plume. The  
 394 median for LSF particle densities is 1.8, 2.0, and 2.0 g/cm<sup>3</sup> in the North Atlantic, SE Pacific, and  
 395 the western Arctic Ocean, respectively. The SSF densities are 2.0±0.4, 1.9±0.4, and 1.9±0.4 g/cm<sup>3</sup>  
 396 (mean±s.d.). Based on the Lilliefors test, only LSF densities in the North Atlantic are normally  
 397 distributed at the 5% significance level. In contrast, all SSF particle densities have normal  
 398 distributions. The North Atlantic has the lowest LSF densities compared to the other two cruises  
 399 ( $p<<0.001$ ), but its SSF densities are significantly higher than the western Arctic Ocean (t-test;  
 400  $p<0.01$ ). Such contrasting characteristics between size fractions can be partly explained by the  
 401 abundance of POM and the lack of opal in the North Atlantic in the LSF (Figures S2g, S2i, &S3).

402 Both the magnitude and variations of seawater densities are small compared to the particle  
 403 density in most cases, which leads to relatively consistent differences between particle density and  
 404 excess densities (Figure S4). Variations in the excess density are controlled by composition effects  
 405 on particle density, not by variations in the seawater density.



407  
 408 Figure 3. LSF (>51 µm) and SSF (1-51 µm) particle densities (unit: g/cm<sup>3</sup>) in three cruises. (a):  
 409 GA03 LSF; (b): GA03 SSF; (c): GP16 LSF; (d): GP16 SSF; (e): GN01 LSF; (f): GN01 SSF. The  
 410 top panel in each subplot is the upper 500 m, and the lower panel is the entire water column. Pump

411 sampling depths with actual data are shown with colored dots outlined in gray, on top of  
 412 interpolated values that are plotted on model grids. Both actual and interpolated values are assigned  
 413 with the same color bar. Thick white contours are potential density anomaly of 25, 26 and 27  
 414 kg/m<sup>3</sup>, and thin white lines are 50 evenly spaced contour lines within the range of the color scale.  
 415 In GN01, northbound and southbound legs are connected, and the North Pole station (90°N) is  
 416 shown in the center.

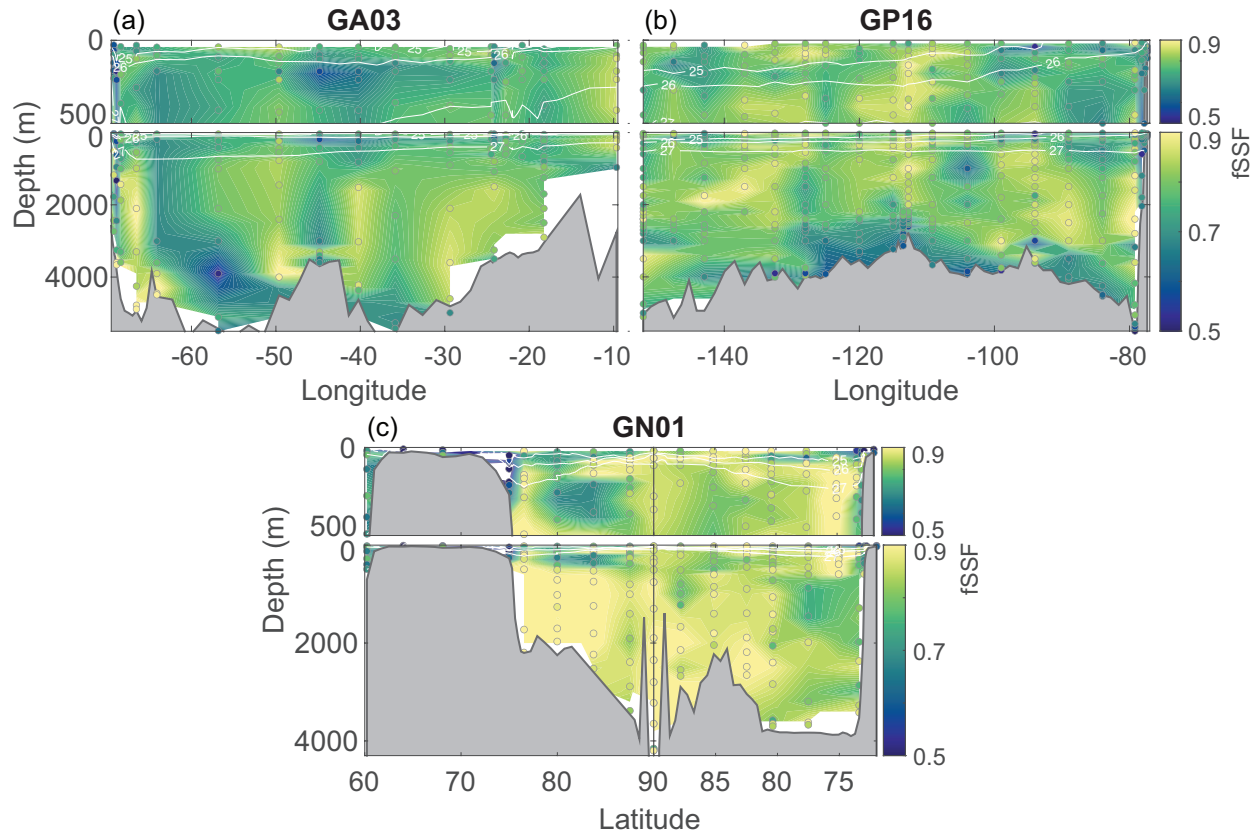
417

### 418 3.4 Mass partitioning

#### 419 3.4.1 The fraction of mass concentrations in the SSF and LSF

420 The SSF SPM generally makes up more TOT SPM concentrations than the LSF (Figure 4).  
 421 A higher fraction of small particles with respect to total mass concentrations (fSSF) corresponds  
 422 to a higher power q in the mass-size spectra. The median (range) fSSF fractions are 76.6% (34.2-  
 423 97.8%), 78.4% (48.4-93.9%), and 85.5% (11.1-96.5%) in the North Atlantic, SE Pacific, and the  
 424 western Arctic Ocean, respectively. The highest fSSF of 97.8% appears in the BNLs along the  
 425 western boundary in the North Atlantic (Figure 4a). Close to the venting site of the EPR  
 426 hydrothermal plume, the fSSF is about 70%, implying hydrothermal particles from the EPR  
 427 partition less towards the SSF than outside the plume (Figure 4b) (Lee et al., 2018). The central  
 428 Arctic Basin is characterized by significantly higher fSSF (more small particles) than the North  
 429 Atlantic and SE Pacific ( $p < < 0.001$ ) (Figure 4c), consistent with oligotrophic conditions and  
 430 subsurface lateral transport of fine particles in the western Arctic Ocean (Xiang & Lam, 2020).  
 431 Interestingly, the lowest fSSF and thereby the largest particles are also in the western Arctic Ocean,  
 432 but over the productive Chukchi Shelf (Figure 4c).

433



434

435 Figure 4. Fraction of SSF in TOT ( $>1 \mu\text{m}$ ) mass concentrations in three cruises. (a): GA03; (b):  
436 GP16; (c) GN01. The top panels in each subplot is the upper 500 m, and the lower panel is the  
437 entire water column.

438

### 439 3.4.2 The mass-size spectra power q

440 Another means to assess the mass partitioning in size-fractionated particles is to compare  
441 the magnitude of the power q in the mass-size spectra (Eq. 8). A higher q indicates more mass  
442 distributed to the SSF compared to the LSF. The mass-size spectra formulation also facilitates  
443 subsequent calculations of sinking velocities (see section 2.6). The distributions of the two  
444 parameters, fSSF and q, look alike (Figures 4 & S5). The medians (ranges) of q are 1.3 (0.9-2.0),  
445 1.3 (1.0-1.7), 1.5 (0.6-1.8) in the North Atlantic, SE Pacific, and the western Arctic Ocean,  
446 respectively.

447

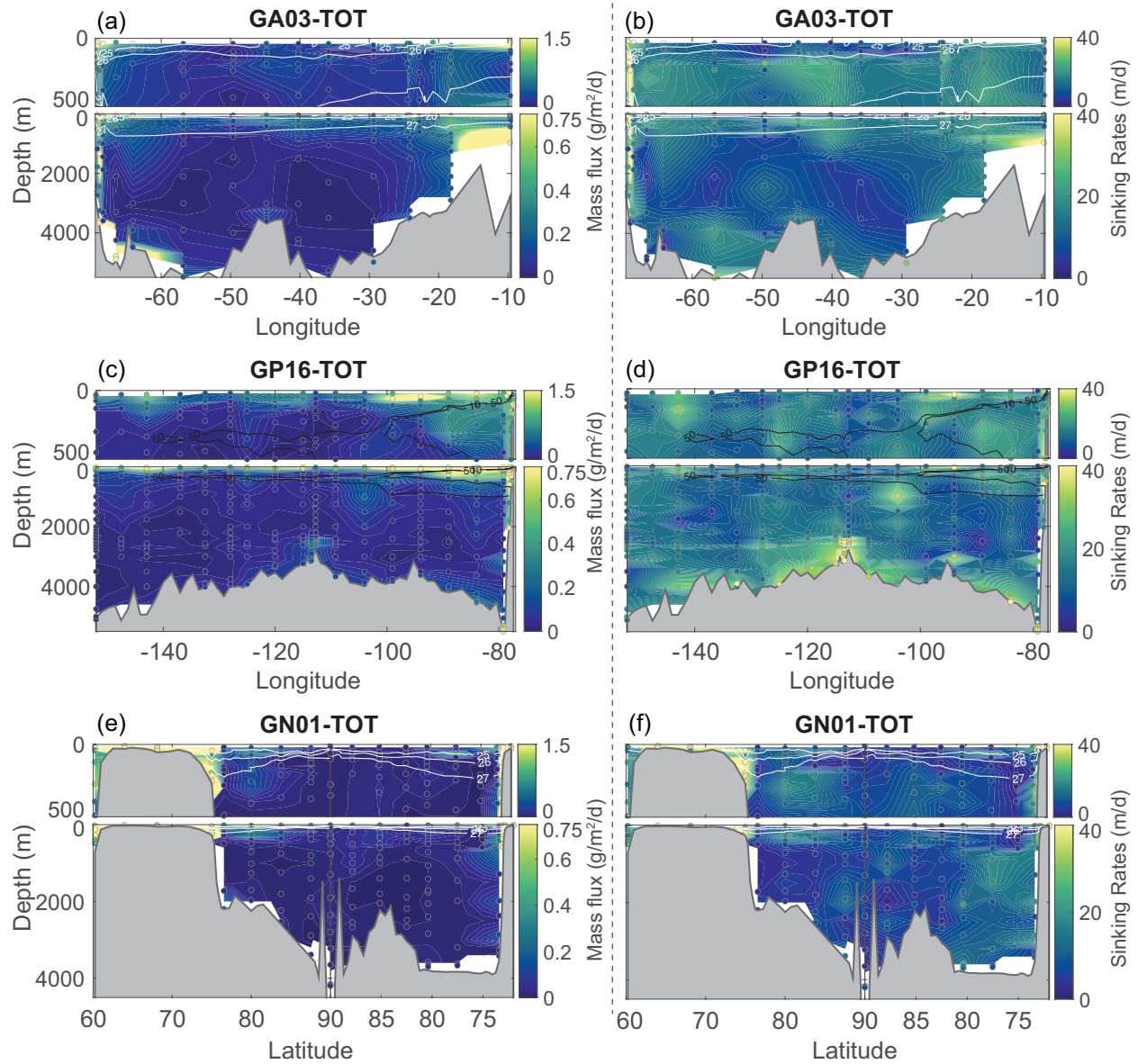
## 448 3.5 Derived variables

### 449 3.5.1 Derived mass flux

450 The LSF mass flux generally decreases with depth and away from the margins, with values  
451 ranging over three to four orders of magnitude within each cruise. The medians (5<sup>th</sup> to 95<sup>th</sup>  
452 percentile range) of LSF mass flux are  $2.0 \times 10^{-1} \text{ g/m}^2/\text{d}$  ( $2.1 \times 10^{-2}$ - $1.9 \text{ g/m}^2/\text{d}$ ) in the North  
453 Atlantic,  $8.9 \times 10^{-2} \text{ g/m}^2/\text{d}$  ( $2.3 \times 10^{-2}$ - $1.0 \text{ g/m}^2/\text{d}$ ) in the SE Pacific, and  $4.4 \times 10^{-2} \text{ g/m}^2/\text{d}$  ( $8.2 \times 10^{-3}$ -  
454  $8.7 \text{ g/m}^2/\text{d}$ ) in the western Arctic Ocean (Figure S6). In terms of 0-100% range of mass flux over  
455 all cruises, it is worth noting that samples with the highest ( $88.2 \text{ g/m}^2/\text{d}$ ) and lowest  
456 ( $2.9 \times 10^{-3} \text{ g/m}^2/\text{d}$ ) mass flux are both in the western Arctic Ocean. The BNLs along the western  
457 boundary in the North Atlantic increase the LSF mass flux to about  $3.5 \text{ g/m}^2/\text{d}$ . In the SSF, the  
458 mass flux varies one to two orders of magnitude within each cruise. The medians (5<sup>th</sup>-95<sup>th</sup>) of SSF  
459 mass flux are  $1.6 \times 10^{-2} \text{ g/m}^2/\text{d}$  ( $4.5 \times 10^{-3}$ - $8.3 \times 10^{-2} \text{ g/m}^2/\text{d}$ ) in the North Atlantic,  $6.5 \times 10^{-3} \text{ g/m}^2/\text{d}$   
460 ( $2.7 \times 10^{-3}$ - $4.4 \times 10^{-2} \text{ g/m}^2/\text{d}$ ) in the SE Pacific, and  $4.9 \times 10^{-3} \text{ g/m}^2/\text{d}$  ( $1.5 \times 10^{-3}$ - $2.7 \times 10^{-1} \text{ g/m}^2/\text{d}$ ) in  
461 the western Arctic Ocean (Figure S6). Fluxes of more than  $1.0 \text{ g/m}^2/\text{d}$  are rare in the SSF, only  
462 occurring in prominent BNLs, such as on the western margin in the North Atlantic and the Chukchi  
463 Shelf in the western Arctic Ocean.

464 The distribution of TOT mass fluxes is similar to the LSF (Figures 5 & S6). The medians  
465 (5<sup>th</sup>-95<sup>th</sup>) of TOT mass flux are  $2.1 \times 10^{-1} \text{ g/m}^2/\text{d}$  ( $2.5 \times 10^{-2}$ - $2.5 \text{ g/m}^2/\text{d}$ ) in the North Atlantic,  
466  $9.7 \times 10^{-2} \text{ g/m}^2/\text{d}$  ( $2.7 \times 10^{-2}$ - $1.1 \text{ g/m}^2/\text{d}$ ) in the SE Pacific, and  $4.9 \times 10^{-2} \text{ g/m}^2/\text{d}$  ( $1.1 \times 10^{-2}$ - $9.6$   
467  $\text{g/m}^2/\text{d}$ ) in the western Arctic Ocean (Figure 5). The highest (100<sup>th</sup> percentile) TOT mass flux is  
468 over the Chukchi Shelf, reaching  $89.6 \text{ g/m}^2/\text{d}$ . The North Atlantic is characterized by the highest  
469 TOT mass flux (Figure 5a), and the western Arctic Ocean has the lowest TOT mass flux  
470 ( $p < 0.001$ ) (Figure 5e). It is interesting that high mass fluxes in the upper 500 m near the Peru  
471 margin persist hundreds of kilometers offshore in the SE Pacific, coinciding with the  $10 \mu\text{mol/kg}$   
472 dissolved oxygen contour line (Figure 5c). The low attenuation of mass flux in this region is  
473 consistent with conclusions drawn from other tracers from the same cruise, such as the  $^{230}\text{Th}$ -  
474 normalized POC flux and stable isotope of nitrate ( $\delta^{15}\text{N}_{\text{NO}_3}$ ), which both point to less POC  
475 regeneration within the Peru oxygen deficient zone (Pavia et al., 2019; Peters et al., 2018).

476



477  
478 Figure 5. Derived mass flux (unit:  $\text{g}/\text{m}^2/\text{d}$ ) in TOT particles (a, c, e), and derived mass-weighted  
479 average sinking velocity (unit:  $\text{m}/\text{d}$ ) in TOT particles in three cruises (b, e, f). (a)-(b): GA03; (c)-  
480 (d): GP16; (e)-(f): GN01. Thick white contours are potential density anomaly of 25, 26 and 27  
481  $\text{kg}/\text{m}^3$ , and thick black contours in the GP16 are dissolved oxygen concentrations of 10 and 50  
482  $\mu\text{mol}/\text{kg}$ . Note that color scales are the same for all cruises but are different between the upper 500  
483 m (top panels) and the whole water column (bottom panels) in the TOT mass flux.  
484

### 485 3.5.2 Derived mass-weighted average sinking velocities

486 The magnitude of mass-weighted average sinking velocities (WSVs) for each size fraction  
487 is determined by the mass fraction and sinking velocity for each size bin (Eq. 12). Sinking  
488 velocities, in turn, are dependent on the hydrography, particle composition, and porosity-size  
489 relationship. The medians ( $5^{\text{th}}\text{-}95^{\text{th}}$  range) of WSVs over all cruises are 60.6  $\text{m}/\text{d}$  (27.0–103.8  $\text{m}/\text{d}$ )  
490 in the LSF, and 1.4  $\text{m}/\text{d}$  ( $4.1 \times 10^{-1}$ –2.6  $\text{m}/\text{d}$ ) in the SSF (Figure S7). Unlike the mass flux, where  
491 the total flux was similar to the LSF flux, WSVs in total particles are less similar to the LSF WSVs:

492 the TOT sinking rates fall between the SSF and LSF, with the median (5<sup>th</sup>-95<sup>th</sup>) of 13.5 m/d (3.4-  
493 41.0 m/d) (Figure 5). This is because the WSVs are an average sinking speed weighted by mass,  
494 thus giving more weight to the slowly sinking particles of the more abundant SSF. In contrast, flux  
495 is simply integrated across sizes, and the larger size range and faster sinking speeds of the LSF  
496 dominate the total flux. In general, we did not find strong evidence for an increasing sinking  
497 velocity with depth, in line with observations by Xue and Armstrong (2009) and Nowald et al.  
498 (2009).

499 The LSF WSVs are high near shelf/slope regions in the North Atlantic, but relatively low  
500 in the surface and deep basin (Figure S7a). The SE Pacific has relatively uniform distributions of  
501 LSF WSVs (Figure S7c). The median (5<sup>th</sup>-95<sup>th</sup>) of LSF WSVs in the SE Pacific is 65.7 m/d (42.8-  
502 113.0 m/d), not significantly different from the North Atlantic ( $p>0.05$ ), which has the median  
503 (5<sup>th</sup>-95<sup>th</sup>) of 62.9 m/d (19.5-118.3 m/d). Interestingly, despite having significantly higher LSF  
504 particle densities compared to the North Atlantic, the Arctic Ocean is characterized by the lowest  
505 LSF sinking rates in all three basins ( $p<<0.001$ ) (Figure S7e). The median (5<sup>th</sup>-95<sup>th</sup>) in the LSF in  
506 the western Arctic Ocean is 46.1 m/d (23.3-90.5 m/d). In this case, the smaller particle size  
507 distribution (Figures 4&S5) and greater importance of viscosity relative to gravitational sinking  
508 (see section 4.3.2.2) in the western Arctic Ocean may play a more important role in diminishing  
509 sinking velocity.

510 Similar to the LSF, the western Arctic Ocean is also characterized by the lowest WSVs in  
511 the SSF ( $p<<0.001$ ), and the median (5<sup>th</sup>-95<sup>th</sup>) is 1.0 m/d ( $2.4\times10^{-1}$ -2.1 m/d) (Figure S7f).  
512 However, unlike for the LSF, the SSF WSVs are relatively high in the deep North Atlantic  
513 compared to the other basins (Figure S7b). The SSF WSVs in the SE Pacific (median: 1.4 m/d;  
514 5<sup>th</sup>-95<sup>th</sup>:  $6.4\times10^{-1}$ -2.7 m/d) are significantly lower than the North Atlantic (median: 1.7 m/d; 5<sup>th</sup>-  
515 95<sup>th</sup>:  $8.8\times10^{-1}$ -2.7 m/d) ( $p<<0.001$ ) (Figure S7d).

516 The median (5<sup>th</sup>-95<sup>th</sup>) of TOT WSVs is 15.4 (4.1-52.2 m/d), 15.2 (6.6-37.0 m/d), and 7.4  
517 m/d (2.3-39.1 m/d) in the North Atlantic, SE Pacific, and the western Arctic Ocean, respectively  
518 (Figure 5). In the central North Atlantic, the TOT WSVs have surface and deep minima of less  
519 than 10 m/d (Figure 5b). As a consequence of a dominance of very small particles in the BNLs,  
520 the TOT WSVs along the deep western boundary are lower than the midwater column values  
521 despite much higher fractions of lithogenic contents. Within the near-field EPR hydrothermal  
522 plume (<80 km from the ridge axis) in the SE Pacific, the TOT WSVs can reach more than 50 m/d  
523 (Figure 5d) owing to increasing particle densities (Figure 3b) from the high oxide fraction (Figure  
524 S2a-b) and lower fSSF (more large particles) (Figure 4b). The most pronounced gradient in TOT  
525 WSVs between the shelf/slope and basin is observed in the western Arctic Ocean (Figure 5f).  
526 Overall, the TOT WSVs in the western Arctic Ocean are significantly lower than the other two  
527 oceans ( $p<<0.001$ ).  
528

## 529 **4. Discussion**

### 530 4.1 Sensitivity tests

531 Sensitivity tests are conducted with different numbers of size bins, upper size limits for the  
532 LSF, and porosity-size relationships. Compared to the latter two, the number of bins is of minor  
533 importance in the variations of mass flux and WSVs, and not discussed here. Additionally,  
534 according to Eq. 13, for given SPM concentrations, the variability is the same between mass flux  
535 and WSVs. Therefore, we only discuss changes in the mass flux term in sensitivity tests below.

536        The mass-size spectra (Eq. 8) change slightly with different upper size limits in the LSF.  
537        The difference in the power  $q$  is generally <1.5% if 10 mm is used as the upper size boundary  
538        instead of 5 mm. However, mass flux is sensitive to the variations in the upper limit in the LSF.  
539        Using the data from the SE Pacific as an example, if setting the upper size boundary as 10 mm  
540        rather than 5 mm, the TOT mass flux and WSVs are both elevated. The absolute difference ranges  
541        from  $1.4 \times 10^{-3}$  to  $1.9 \text{ g/m}^2/\text{d}$  and the median is  $3.0 \times 10^{-2} \text{ g/m}^2/\text{d}$  (Figure S8a). The percentage of  
542        increase has a median (range) of 30.1% (4.3%-58.9%).

543        The mass flux is also very sensitive to the choice of the porosity-size relationship. As seen  
544        in Figure 2, the power-law relationship in the Alldredge and Gotschalk (1988) (P1) has a steeper  
545        slope and higher coefficient than the new compilation used in this paper (P2). For particle sizes  
546        below 5 mm, the P1 relationship tends to have a higher 1-P, thereby lower P, which leads to higher  
547        mass fluxes. If keeping the upper size limit in the LSF as 5 mm, the TOT mass flux derived from  
548        the P1 changes by a median of  $1.5 \times 10^{-1} \text{ g/m}^2/\text{d}$  and 156.7% in the absolute and relative increase,  
549        respectively, when compared to ones calculated using the P2 relationship (Figure S8b).

550

#### 551 4.2 Literature comparisons

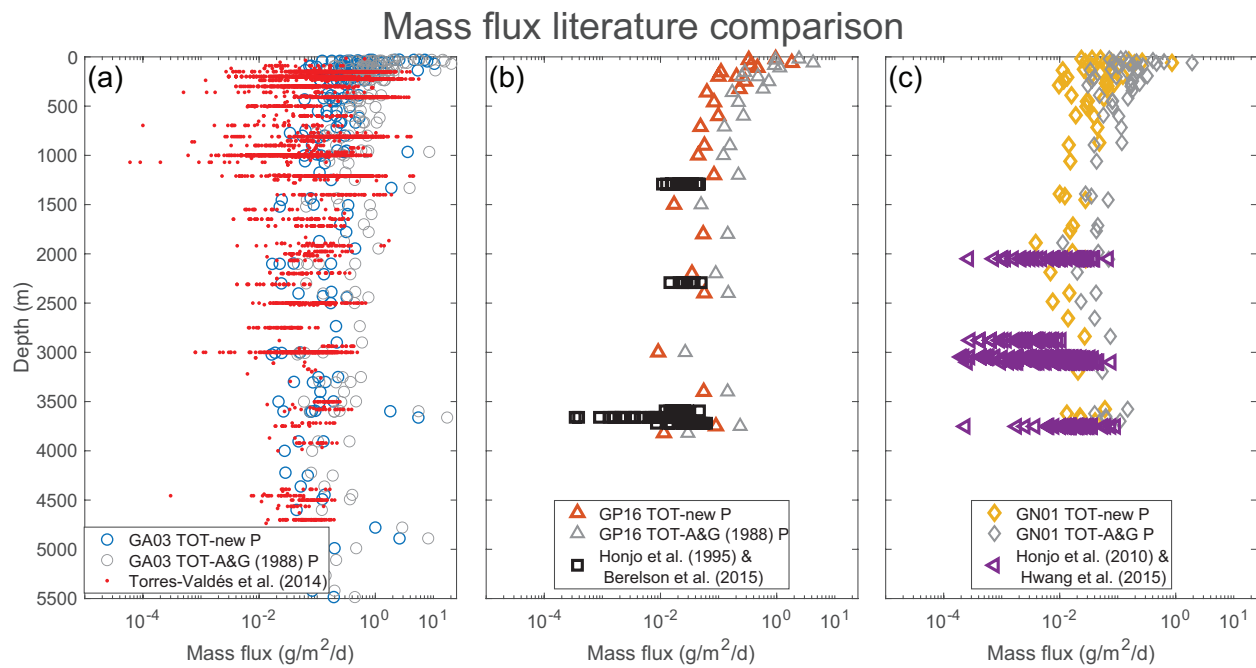
552        Most observations of mass fluxes are from sediment traps. Particles collected by sediment  
553        traps and large-volume in-situ pumps, however, integrate over different temporal and spatial  
554        scales. Moored sediment traps are usually deployed for weeks and months, neutrally buoyant or  
555        surface-drifting traps are deployed for days, whereas pumps collect particles for several hours.  
556        Longer deployment times allow sediment traps to capture rare fast-sinking particles, but sediment  
557        traps tend to undercollect slowly-sinking particles owing to hydrodynamic discrimination  
558        (Gustafsson et al., 2004). Pumps sample abundant slowly-sinking particles well, but are less likely  
559        to capture rare, fast-sinking particles. Despite the sampling differences, derived TOT mass fluxes  
560        using the pump data in this study are comparable to existing sediment trap studies (Figure 6)  
561        (Berelson et al., 2015; Honjo et al., 1995; Honjo et al., 2010; Hwang et al., 2015; Torres-Valdés  
562        et al., 2014). Note that there are fewer sediment trap studies in the South Pacific and Arctic Oceans  
563        as there are in the North Atlantic. Mass fluxes derived from the newly compiled P2 porosity-size  
564        power function are closer to sediment trap observations than those using the original P1  
565        relationship. The difference in mass flux between the two porosity-size relationships results from  
566        higher porosity for all particles  $>8.6 \mu\text{m}$  in the P2 relationship, given an upper size limit of 5 mm  
567        in our current study.

568        Existing measurements of sinking velocities of natural marine particles, direct or indirect,  
569        vary by several orders of magnitude, ranging from several meters to thousands of meters per day  
570        (Alldredge & Gotschalk, 1988; Alonso-González et al., 2010; Armstrong et al., 2009; Bach et al.,  
571        2016; Bach et al., 2019; Berelson, 2001; Briggs et al., 2020; Estapa et al., 2019; Giering et al.,  
572        2016; McDonnell & Buesseler, 2010; McDonnell & Buesseler, 2012; Nowald et al., 2009;  
573        Peterson et al., 2005; Pilskaln et al., 1998; Riley et al., 2012; Trull et al., 2008; Turner, 2002). Our  
574        estimates of TOT WSVs, about  $10\text{-}30 \text{ m/d}$  (Figure 5), fall within the range of 2 to  $54 \text{ m/d}$  measured  
575        using gel traps and in situ camera system for particles between  $73$  and  $1400 \mu\text{m}$  at the Bermuda  
576        Atlantic Time-Series (BATS) in the Sargasso Sea (McDonnell & Buesseler, 2012). The TOT  
577        WSVs, however, are almost an order of magnitude higher than  $2\text{-}3 \text{ m/d}$  estimated using a thorium  
578        ( $\text{Th}$ ) based inverse method in the North Atlantic (Lerner et al., 2017). Approximations of the  
579        sinking velocity derived from  $^{230}\text{Th}$  observations are also about  $1\text{-}3 \text{ m/d}$  in other parts of the ocean  
580        (Bacon & Anderson, 1982; Krishnaswami et al., 1981; Rutgers van der Loeff & Berger, 1993;  
581        Scholten et al., 1995). Puigcorbé et al. (2015) estimated the sinking velocity of total particles as

582 5±2 m/d based on  $^{234}\text{Th}$  data collected with pumps in the Northeast Pacific. In general, the SSF  
 583 WSVs (~1-3 m/d) are much closer to the values from these Th-based estimates compared to the  
 584 TOT WSVs (~10-30 m/d). Burd et al. (2007) pointed out that bulk measurements such as  
 585 particulate  $^{234}\text{Th}$  are likely to represent the properties of small particles more than large particles.  
 586 Adsorption of radionuclides such as thorium is a function of available particle surface area (e.g.,  
 587 Santschi et al., 2006), and should thus be weighted to small particles that have higher surface area  
 588 to volume ratios. In contrast, in our method, mass flux and WSVs are both mass-based and derived  
 589 from the particle volume (Eqs. 11&12), which gives more importance to larger particles and thus  
 590 a higher total sinking velocity.

591 Alternative chemical tracers, such as chloropigments, have also been used with inverse  
 592 models to calculate sinking velocities for different size pools. Indeed, sinking rate estimates from  
 593 a recent chloropigments-based inverse method by Wang et al. (2019) using data from in-situ pumps  
 594 in the Mediterranean Sea are in good agreement with our study. Their modeled sinking velocities  
 595 are  $66.8 \pm 68.6$  m/d (mean±s.d.) for large particles ( $>70 \mu\text{m}$ ), with a range between 7 to 183 m/d,  
 596 and  $1.8 \pm 1.9$  m/d, for small particles ( $1-70 \mu\text{m}$ ), ranging between 0.2-5 m/d.

597



598  
 599 Figure 6. Comparisons between pump-derived and sediment trap-measured TOT mass flux (unit:  
 600  $\text{g}/\text{m}^2/\text{d}$ ) in three cruises. (a): GA03; (b): GP16; (c): GN01. Mass fluxes calculated from the  
 601 porosity-size relationship in Alldredge and Gotschalk (1988) are in gray. All GA03 stations are  
 602 used to compared with data from Torres-Valdés et al. (2014), which covers both North and South  
 603 Atlantic and includes many types of sediment traps. Only Stations 13-14 and 29-30 in the GP16  
 604 are used in (b) to compare with Station 12 in Honjo et al. (1995) and Stations 5 and 7 in Berelson  
 605 et al. (2015). The TOT mass flux in Stations 46-56 in the Canada Basin in the GN01 are shown in  
 606 (c). Sediment traps in both Honjo et al. (2010) and Hwang et al. (2015) were deployed at  $75^\circ\text{N}$ ,  
 607  $150^\circ\text{W}$  in the center of Canada Basin.

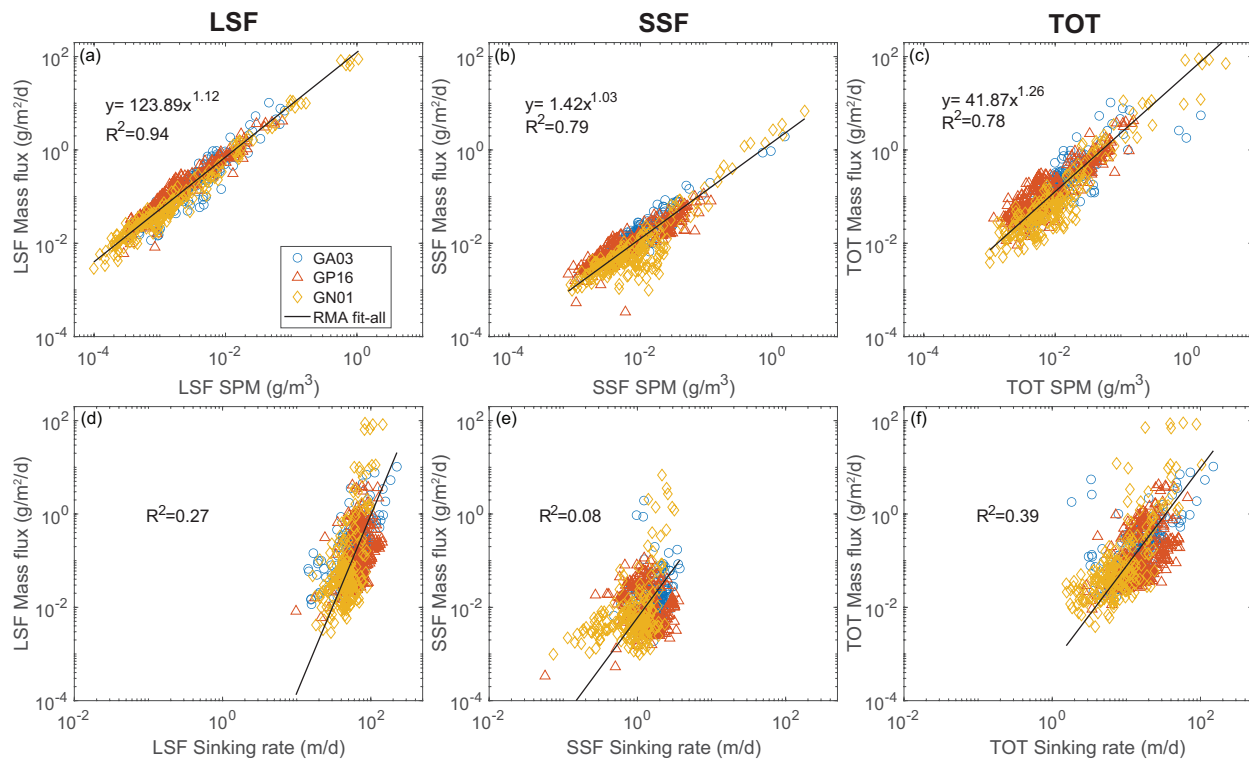
608

609 4.3 Controls on the mass flux

610        The mass flux is calculated as the product of the particle concentration and sinking velocity.  
 611        Sinking velocity, in turn, depends on composition, size, and hydrography (g, viscosity, and  
 612        seawater density). Previous work has mostly focused on different factors impacting particle  
 613        sinking velocities, such as the role of particle size (Alldredge & Gotschalk, 1988; Engel et al.,  
 614        2009; Guidi et al., 2008; Iversen & Ploug, 2010; Iversen & Robert, 2015; Laurenceau-Cornec et  
 615        al., 2020; Laurenceau-Cornec et al., 2015b; McDonnell & Buesseler, 2010; Schmidt et al., 2014),  
 616        particle composition (Bach et al., 2016; Bach et al., 2019; Engel et al., 2009; Laurenceau-Cornec  
 617        et al., 2020; Laurenceau-Cornec et al., 2015b; Schmidt et al., 2014), and the hydrographic effects  
 618        owing to the density discontinuities (Alldredge et al., 2002; Alldredge & Crocker, 1995; Kindler  
 619        et al., 2010; MacIntyre et al., 1995; Prairie et al., 2013; Prairie et al., 2015). Our comprehensive  
 620        work examines all of these components governing the mass flux and adds valuable in-situ particle  
 621        composition data to the existing literature.  
 622

#### 623 4.3.1 Effects of particle concentration and weighted sinking velocities on mass flux

624        The SPM concentrations and weighted sinking velocities are used to calculate the mass  
 625        flux (Eq. 13). Of these two factors, the mass flux is better correlated with SPM than with WSVs  
 626        (Figure 7), with the relationships best for the LSF.  
 627



628        Figure 7. Relationships between size-fractionated SPM concentrations and mass flux (a-c), and  
 629        between mass-weighted average sinking velocity (WSVs) and mass flux (d-f). The (a) and (d) are  
 630        LSF, (b) and (e) are SSF, (c) and (f) are TOT. All the x and y are in logarithmic scale. The reduced  
 631        major axis (Model II linear fit) is used in the regression. Regression equations are displayed in (a)-  
 632        (c), whereas only the coefficient of determination  $R^2$  is shown in (d)-(f). All regression fits are  
 633        significant (F-test: degrees of freedom: ~700,  $p < 0.001$ ).  
 634

635

636        The scatter about the relationship between mass flux and SPM reflects the influence of  
637        WSV and therefore in the components (particle composition, size, and hydrography) that  
638        contribute to WSV. The scatter is most evident at the low end in the western Arctic Ocean in the  
639        SSF and TOT. The sections below will discuss how particle size, composition, and hydrography  
640        affects the sinking velocity and thus the mass flux.

641        4.3.1.1 Effects of particle size on sinking velocity

642        It is straightforward to recognize the importance of size in controlling the sinking velocity:  
643        according to Stokes' Law, sinking velocities increase with the square of particle diameter. The size  
644        effect on sinking velocity is highly dependent on the porosity-size relationship, however.  
645        Incorporation of any porosity-size relationship reduces the exponent value in Stokes' Law (Eqs.  
646        3-4), diminishing the importance of particle size. The lower coefficient in the newly compiled  
647        porosity-size relationship increases the importance of porosity for particles as small as 8.6  $\mu\text{m}$ ,  
648        which tends to reduce overall sinking velocities and thus flux compared to the porosity-size  
649        relationship from Alldredge and Gotschalk (1988) (Figure 6). The integration of the new porosity-  
650        size relationship (Figure 2) results in a power of  $\sim 0.8$  applied to particle diameter, which makes  
651        the dependence of sinking velocity less sensitive to changes in size than to changes in density.

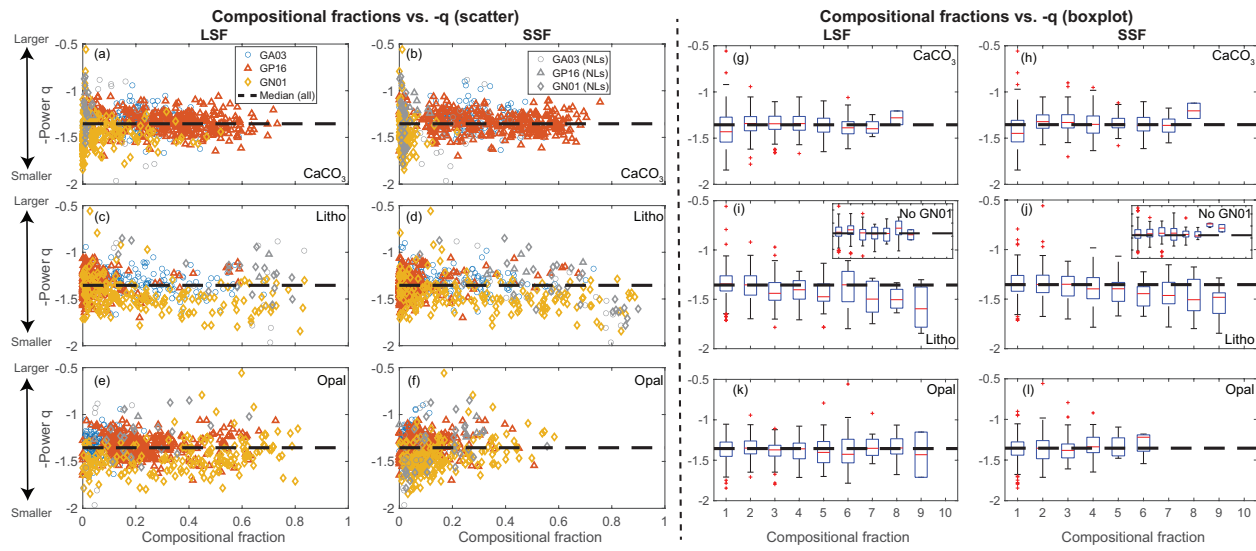
652        Additionally, much lower mass partitioning to large particles further reduces the  
653        significance of particle size on sinking velocity. In our model, the mass fraction decreases with  
654        size due to a negative slope between the mass concentration and size (Eq. 9 & Figure S5). The  
655        WSVs are the sum of sinking velocity in each size bin weighted by its mass fraction (Eq. 12). With  
656        porosity, the last LSF size bin ( $4.2 \times 10^3$ - $5.0 \times 10^3 \mu\text{m}$ ) has sinking velocities of about four orders of  
657        magnitude higher than the first bin in the SSF ( $1.0$ - $1.2 \mu\text{m}$ ), reaching a median of  $3.5 \times 10^2 \text{ m/d}$ . Its  
658        mass fraction, however, is much lower and only accounts for a median of 0.35% in TOT mass  
659        concentrations. Therefore, the effects of particle size on the overall mass flux are much less  
660        important than the classic perspective from Stokes' Law, due to the existence of porosity, as also  
661        proposed by Laurenceau-Cornec et al. (2020), and the dominance of smaller particles.

662        4.3.1.2 Effects of particle composition on sinking velocity

663        Several previous studies have shown that incorporation of minerals, such as lithogenic  
664        particles and  $\text{CaCO}_3$ , decreases particle size (De La Rocha et al., 2008; Engel et al., 2009; Hamm,  
665        2002; Iversen & Ploug, 2010; Laurenceau-Cornec et al., 2020; Nowald et al., 2015; Passow & De  
666        La Rocha, 2006; Passow et al., 2014; Schmidt et al., 2014). Most of these conclusions were drawn  
667        using aggregates formed in lab roller tanks. Natural aggregates may have different behaviors when  
668        exposed to minerals.

669        In our study using natural particles from the full water column, we did not find evidence to  
670        support the role of  $\text{CaCO}_3$  and opal in affecting particle size distribution (Figure 8a-b & e-f). We  
671        do find, however, that the abundance of small particles (denoted by the magnitude of the exponent  
672        q) decreases with lithogenic fraction (Figure 8c-d). This relationship is predominantly driven by  
673        particles in the deep western Arctic Ocean and by the strong bottom nepheloid layers (BNLs) of  
674        the western boundary current in the North Atlantic and Chukchi Shelf (Lam et al., 2015; Xiang &  
675        Lam, 2020). The western Arctic Ocean is heavily influenced by lateral transport from sediment  
676        resuspension over the Chukchi Shelf and Slope, resulting in high fractions of lithogenic particles  
677        below 1000 m (Xiang & Lam, 2020). The association of lithogenic content and small particle size  
678        is thus driven by sediment resuspension processes, and not by a decrease in aggregate size caused  
679        by lithogenic content. If we exclude the entire GN01, small particles in the North Atlantic and SE

682 Pacific outside strong BNLS no longer decrease with the lithogenic fraction (Figure 8i-j). Indeed,  
 683 the abundance of large particles may even increase with the SSF lithogenic fractions. Therefore,  
 684 we postulate that in areas away from sediment resuspension, incorporation of ballast minerals into  
 685 aggregates is not a primary controlling factor on the particle size distribution.  
 686



687  
 688 Figure 8. Scatter (a-f) and box plots (g-l) between size-fractionated (LSF: left; SSF: right)  
 689 compositional fraction and negative power exponent  $q$ ,  $-q$ , in the mass-size spectra. Three major  
 690 ballast minerals,  $\text{CaCO}_3$ , Litho and opal, are shown in the top, middle and bottom panels,  
 691 respectively. The black dashed line is the median of all  $-q$  in each size fraction from all cruises.  
 692 Nepheloid layers (NLS) are defined as any lithogenic concentrations of  $>5 \mu\text{g/L}$  in both size  
 693 fractions and plotted in gray in the scatter plots. Compositional fractions are binned for every 10%  
 694 between 0 and 100% in the box plots, excluding all NLS samples. The red segment inside the  
 695 rectangle indicates the median and whiskers above and below the box show values of the minimum  
 696 and maximum. Outliers are shown with red plus signs. Insets in (i) and (j) are plots excluding data  
 697 from the GN01.  
 698

699 The sinking velocity increases with excess densities on the basis of Stokes' Law. The  
 700 densities of  $\text{Fe(OH)}_3$  and  $\text{MnO}_2$  are higher than  $\text{CaCO}_3$  and lithogenic materials, but they are  
 701 usually a much smaller fraction of the particulate mass (Figures S2-3). A few notable exceptions  
 702 occur in hydrothermal plumes, where they can account for up to 50% of SPM concentrations. The  
 703  $\text{CaCO}_3$  and Litho are often the most important ballast minerals owing to their high densities and  
 704 abundances. The density of POM ( $\sim 1.05 \text{ g/cm}^3$ ) is the lowest among all major phases and similar  
 705 to seawater density ( $\sim 1.03 \text{ g/cm}^3$ ). Given the small value in the excess density, particles with a  
 706 high fraction of POM sink slowly compared to other types.

707 It is worth noting that the opal density,  $\sim 2.0 \text{ g/cm}^3$ , is very similar to the median of overall  
 708 particle densities in the ocean (see section 3.3), which tend to frequently be a mixture of POM and  
 709  $\text{CaCO}_3$  and/or Litho. Additions of opal into marine aggregates would not lead to substantial  
 710 increases in excess densities, thereby sinking velocities, and suggest that opal is likely of minor  
 711 importance in influencing the overall sinking velocity. To increase sinking velocities, particles  
 712 have to be characterized by elevated fractions of  $\text{Fe(OH)}_3$ ,  $\text{MnO}_2$ ,  $\text{CaCO}_3$  or Litho. Our hypothesis  
 713 is consistent with Klaas and Archer (2002) where they explain the low correlation between deep

714 POC and opal fluxes as a consequence of the relatively low density of opal compared to  $\text{CaCO}_3$   
715 and lithogenic particles. The apparent weak ballasting effect of opal has also been attributed to  
716 higher aggregate porosities, reduced aggregate compactness, and increased POC lability (Bach et  
717 al., 2016; Bach et al., 2019; Francois et al., 2002; Lam & Bishop, 2007; Lam et al., 2011). This  
718 work shows that an increase in the fraction of opal is not associated with a higher abundance of  
719 larger particles (Figure 8e-f & k-l). Direct measurements of opal size and porosity in the future are  
720 needed to examine the role of porosity in the opal ballast more carefully.

721 To summarize, we did not observe any obvious decrease in particle size distribution with  
722 incorporation of ballast minerals in natural particles. In this study, effects of particle composition  
723 mainly manifest in density of different phases, where  $\text{CaCO}_3$  and lithogenic particles are generally  
724 the two most important ballast minerals that add excess density to POM. The direct ballast effect  
725 of opal appears to be very weak, given its similar density to median of particle densities. We cannot  
726 exclude other hypotheses for the weak role of opal in particle flux, such as ecosystem effects (Lima  
727 et al., 2014) and POC lability (Lam et al., 2011), however.

728

#### 729 4.3.1.3 Effects of hydrography on sinking velocity

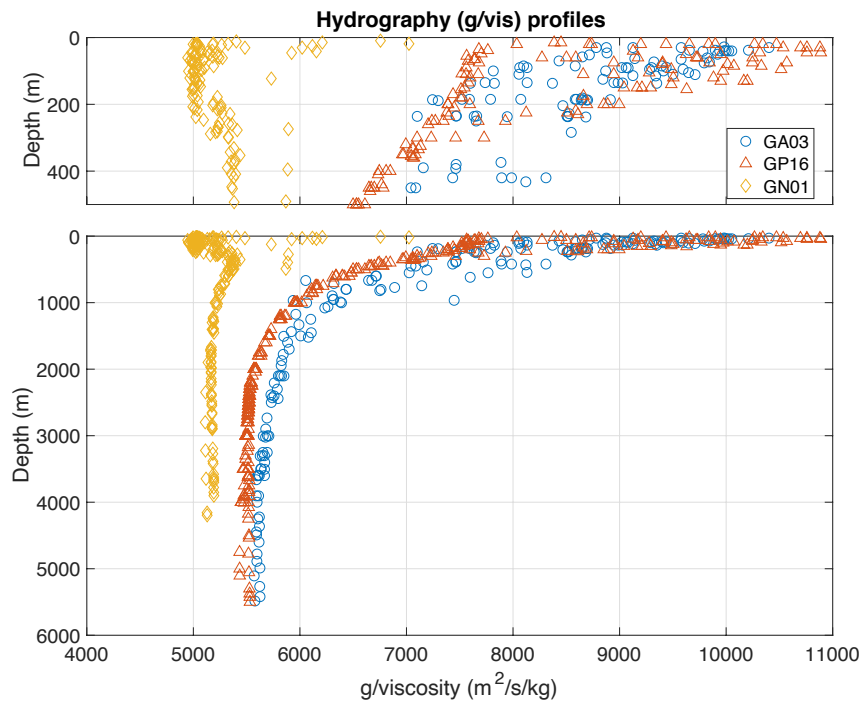
730 Hydrographic parameters in the Stokes' velocity calculation include seawater density,  
731 gravitational acceleration, and viscosity. Strong density gradients appear in the upper water  
732 column in three oceans, especially in the Arctic Ocean. A decrease in sinking velocities and  
733 accumulations of particles within a thin layer of sharp density gradients has been observed for  
734 marine aggregates both in-situ and in laboratory settings (Alldredge et al., 2002; Alldredge &  
735 Crocker, 1995; Kindler et al., 2010; MacIntyre et al., 1995; Prairie et al., 2013; Prairie et al., 2015).  
736 Elevations of beam attenuation from the transmissometer are generally observed within the  
737 pycnocline in all three cruises (Anderson & Fleisher, 2013). Our pump sampling resolution,  
738 however, may not be fine enough to capture such features on the scale of a few meters, given the  
739 absence of obvious elevations in particle concentrations at the density discontinuities.

740 The influence of seawater density is incorporated into the calculation of excess densities,  
741 but as noted previously, variations in seawater density are usually small compared to variation in  
742 particles densities (see section 3.3). Sharp density gradients are generally associated with sharp  
743 viscosity gradients, since both parameters depend on temperature and salinity, so the hydrography  
744 effects on mass flux mainly manifest in the g/viscosity term (Eq. 3). Gravitational acceleration  
745 varies by less than 1% between Arctic and tropical waters. The most variation results from the  
746 viscosity, which is highly temperature-dependent (Millero, 1974). We disregard potential  
747 biological contributions to viscosity such as from the release of mucous materials including  
748 transparent exopolymer particles (TEP) (Jenkinson, 1986; 1993; Jenkinson & Biddanda, 1995;  
749 Seuront et al., 2007; Seuront et al., 2010; Seuront & Vincent, 2008; Seuront et al., 2006).

750 In the western Arctic Ocean, the ratios of g/viscosity (g/vis) are lowest in the surface  
751 ( $\sim 5000 \text{ m}^2/\text{s/kg}$ ), highest at about 300 m below the Pacific-derived halocline ( $\sim 5400 \text{ m}^2/\text{s/kg}$ ), and  
752 remain relatively constant in the deep ocean ( $\sim 5200 \text{ m}^2/\text{s/kg}$ ) (Figure 9). In contrast, g/vis ratios  
753 are highest in the surface North Atlantic and SE Pacific ( $\sim 10000 \text{ m}^2/\text{s/kg}$ ), and decrease rapidly  
754 with depth. Higher values of g/vis in the surface (low viscosity) facilitate particle sinking out of  
755 the surface where remineralization rates are highest. On the basis of g/viscosity profiles alone, one  
756 would expect sinking velocities to slow down with depth in the North Atlantic and SE Pacific,  
757 especially in upper 2000 m, whereas not change much in the western Arctic Ocean. The fact that  
758 WSVs do not decrease with depth in the North Atlantic and SE Pacific (Figures 5b, 5d, & S7a-d)  
759 is caused by generally increasing excess densities with depth (Figure 3). Places with small

760 g/viscosity variations with depth, such as the western Arctic Ocean, however, have more potential  
 761 for increasing excess density to increase sinking velocities with depth.

762 When comparing values of g/vis between three basins, they only differ by <10% in the  
 763 deep ocean, but can be up to 200% different in the upper water column (Figure 9). This distinct  
 764 feature in the high-latitude Arctic Ocean can lead to up to two times smaller sinking velocities and  
 765 mass fluxes than low-latitude oceans, partly contributing to smaller sinking velocities and mass  
 766 fluxes in the upper water column in the Arctic Ocean (Figures S6-S7).



768  
 769 Figure 9. Profiles of hydrographic parameter g/ viscosity (unit:  $\text{m}^2/\text{s}/\text{kg}$ ) in the upper 500 m (top  
 770 panel) and the whole water column (bottom panel) in three cruises.

771  
 772 4.3.2 The relative importance of hydrography, particle concentration, size, and composition for  
 773 mass flux

774 The size-fractionated mass flux is calculated as the sum of mass flux in each size bin (Eq.  
 775 11). Equivalently, it can also be expressed as the product of the overall mass concentration and  
 776 WSVs (Eq. 13). Combining Eqs. 4, 12 and 13, we generate an overall equation with concentration,  
 777 size, composition, and hydrography terms to calculate mass flux (Eq. 14), which can be used to  
 778 quantitatively de-convolve the contribution of each effect to the variability and magnitude of mass  
 779 flux in the SSF and LSF (Table 1).

$$F = \left( \int_{d_1}^{d_2} \frac{m_i}{\int_{d_1}^{d_2} m_i dd} \times (1 - P_i) \frac{g \Delta Q (d_i / 10^6)^2}{18 \eta} dd \right) \times SPM \quad (14)$$

780 We define the concentration effect directly as SPM, and the size effect as  $\int_{d_1}^{d_2} \frac{m_i}{\int_{d_1}^{d_2} m_i dd} \times (1 - P_i) \times (d_i / 10^6)^2 dd$  =  $\int_{d_1}^{d_2} \frac{m_i}{\int_{d_1}^{d_2} m_i dd} \times 3.6 \times 10^{-11.4} \times (d_i)^{0.8} dd$ , which includes both the porosity-size  
 781 relationship and mass partitioning of particles, and is calculated as the sum of contribution from  
 782

783 each size bin. The excess density,  $\Delta\varrho$ , is used to represent the composition effect, and the  
 784 hydrography effect is defined as g/viscosity, g/ $\eta$ . Multiplying all four terms would generate an  
 785 adjusted mass flux that is 18 times higher than the actual derived mass flux (unit: g/m<sup>2</sup>/s). The  
 786 variability and magnitude of individual terms, therefore, are helpful in understanding their relative  
 787 importance in determining mass flux. We only focus on the upper 100 m of the water column of  
 788 all non-shelf stations to assess the importance of these four effects across surface ecosystems. To  
 789 avoid extreme outliers, we use the range between 5 and 95 percentiles in each term to demonstrate  
 790 the variability and magnitude of mass flux.

791

792 **Table 1. The Contributions from Different Factors to the Variation of Mass Flux (<100 m)**

Cruise	Effects	LSF		SSF	
		5-95%ile range (median)	95/5 range ratios	5-95%ile range (median)	95/5 range ratios
GA03	Concentration [unit: g/m <sup>3</sup> ]	$4.1 \times 10^{-3}$ - $6.3 \times 10^{-2}$ $(7.5 \times 10^{-3})$	15.5	$1.4 \times 10^{-2}$ - $4.7 \times 10^{-2}$ $(2.5 \times 10^{-2})$	3.4
	Size [unit: m <sup>2</sup> ]	$2.0 \times 10^{-9}$ - $3.8 \times 10^{-9}$ $(2.4 \times 10^{-9})$	1.9	$4.9 \times 10^{-11}$ - $9.2 \times 10^{-11}$ $(5.9 \times 10^{-11})$	1.9
	Composition [unit: kg/m <sup>3</sup> ]	$1.5 \times 10^{-2}$ - $9.5 \times 10^{-2}$ $(4.9 \times 10^{-2})$	6.3	$2.5 \times 10^{-2}$ - $9.0 \times 10^{-2}$ $(4.5 \times 10^{-2})$	3.5
	Hydrography [unit: m <sup>2</sup> /s/kg]	$8.1 \times 10^{-3}$ - $1.0 \times 10^{-4}$ $(9.4 \times 10^{-3})$	1.3	$8.1 \times 10^{-3}$ - $1.0 \times 10^{-4}$ $(9.4 \times 10^{-3})$	1.3
GP16	Concentration [unit: g/m <sup>3</sup> ]	$2.6 \times 10^{-3}$ - $2.3 \times 10^{-2}$ $(7.7 \times 10^{-3})$	9.1	$1.7 \times 10^{-2}$ - $5.9 \times 10^{-2}$ $(2.9 \times 10^{-2})$	3.5
	Size [unit: m <sup>2</sup> ]	$1.7 \times 10^{-9}$ - $2.7 \times 10^{-9}$ $(2.2 \times 10^{-9})$	1.6	$4.1 \times 10^{-11}$ - $6.6 \times 10^{-11}$ $(5.3 \times 10^{-11})$	1.6
	Composition [unit: kg/m <sup>3</sup> ]	$4.9 \times 10^{-2}$ - $1.2 \times 10^{-3}$ $(6.5 \times 10^{-2})$	2.4	$2.1 \times 10^{-2}$ - $5.9 \times 10^{-2}$ $(3.1 \times 10^{-2})$	2.8
	Hydrography [unit: m <sup>2</sup> /s/kg]	$7.7 \times 10^{-3}$ - $1.1 \times 10^{-4}$ $(9.7 \times 10^{-3})$	1.4	$7.7 \times 10^{-3}$ - $1.1 \times 10^{-4}$ $(9.7 \times 10^{-3})$	1.4
GN01	Concentration [unit: g/m <sup>3</sup> ]	$8.7 \times 10^{-4}$ - $3.9 \times 10^{-2}$ $(3.0 \times 10^{-3})$	44.8	$8.4 \times 10^{-3}$ - $8.6 \times 10^{-2}$ $(1.5 \times 10^{-2})$	10.2
	Size [unit: m <sup>2</sup> ]	$1.4 \times 10^{-9}$ - $3.1 \times 10^{-9}$ $(2.0 \times 10^{-9})$	2.2	$3.3 \times 10^{-11}$ - $7.6 \times 10^{-11}$ $(4.9 \times 10^{-11})$	2.3
	Composition [unit: kg/m <sup>3</sup> ]	$4.2 \times 10^{-2}$ - $1.3 \times 10^{-3}$ $(6.8 \times 10^{-2})$	3.0	$1.3 \times 10^{-2}$ - $9.3 \times 10^{-2}$ $(2.9 \times 10^{-2})$	7.0
	Hydrography [unit: m <sup>2</sup> /s/kg]	$5.0 \times 10^{-3}$ - $5.3 \times 10^{-3}$ $(5.1 \times 10^{-3})$	1.1	$5.0 \times 10^{-3}$ - $5.3 \times 10^{-3}$ $(5.1 \times 10^{-3})$	1.1
Global	Concentration [unit: g/m <sup>3</sup> ]	$9.8 \times 10^{-4}$ - $4.1 \times 10^{-2}$ $(6.5 \times 10^{-3})$	42.1	$9.3 \times 10^{-3}$ - $5.3 \times 10^{-2}$ $(2.4 \times 10^{-2})$	5.7
	Size [unit: m <sup>2</sup> ]	$1.6 \times 10^{-9}$ - $3.2 \times 10^{-9}$ $(2.3 \times 10^{-9})$	2.0	$3.9 \times 10^{-11}$ - $7.7 \times 10^{-11}$ $(5.5 \times 10^{-11})$	2.0
	Composition [unit: kg/m <sup>3</sup> ]	$2.8 \times 10^{-2}$ - $1.1 \times 10^{-3}$ $(6.5 \times 10^{-2})$	4.1	$1.6 \times 10^{-2}$ - $7.7 \times 10^{-2}$ $(3.5 \times 10^{-2})$	4.9
	Hydrography [unit: m <sup>2</sup> /s/kg]	$5.0 \times 10^{-3}$ - $1.1 \times 10^{-4}$ $(8.9 \times 10^{-3})$	2.1	$5.0 \times 10^{-3}$ - $1.1 \times 10^{-4}$ $(8.9 \times 10^{-3})$	2.1

793

#### 794 4.3.2.1 Effects on variability of mass flux

795 The variability of mass flux within each size fraction with respect to hydrography, particle  
 796 concentration, size, and composition is first evaluated by examining the ratio of the 95<sup>th</sup> to 5<sup>th</sup>  
 797 percentile values for each of these four effects as defined above (Table 1). This 95<sup>th</sup> to 5<sup>th</sup>

percentile ratio is a metric we use to quantify the observed variability in these effects, and thus assess the expected influence each effect may have on the observed variability in mass flux.

SPM shows the highest ratio of the 95<sup>th</sup> to 5<sup>th</sup> percentiles in all three cruises, and thus accounts for most of the variability in the mass flux, consistent with good correlations between SPM concentration and mass flux (Figures 7a-c, 10a-b). The concentration range ratio in the western Arctic Ocean (44.8 and 10.2 for LSF and SSF, respectively) is much higher than other oceans, demonstrating the enormous SPM range sampled on that cruise (Figure 10a-b). Given the much higher SPM concentrations on the Chukchi Slope, we also calculated the ratio between 90 and 5 percentiles for both size fractions in the western Arctic Ocean, and they are 19.2 and 3.0 for the LSF and SSF, respectively. The adjusted LSF ratio in the western Arctic Ocean is still the highest among all cruises, whereas the SSF is similar to the North Atlantic and SE Pacific.

The composition effect has the second highest ratio of the 95<sup>th</sup> to 5<sup>th</sup> percentiles. In the North Atlantic, the SSF range ratio for composition is slightly higher than that in the concentration. Particle composition differences may thus be more important than concentration differences for explaining mass flux variability in the SSF.

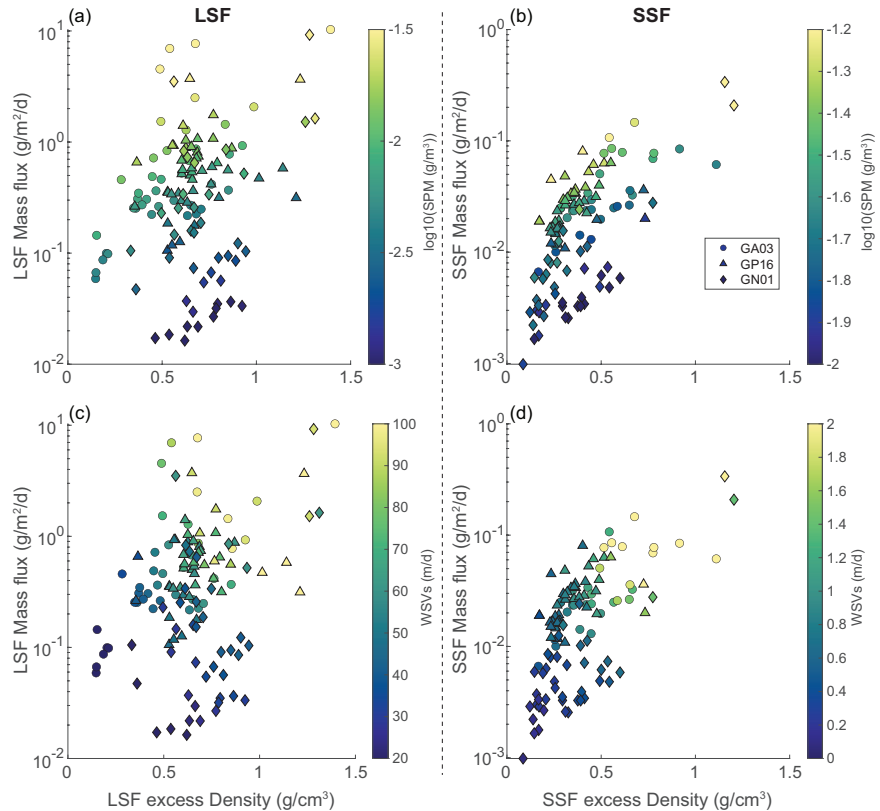
Surprisingly, the range of variability as a result of the size effect is relatively low in both size fractions, about 1-3 times lower than the composition effect. Despite the strong  $d_i^2$  size dependence in the size term in the Stokes equation, the incorporation of size-dependent porosity reduces this effect to a dependency on  $d_i^{0.8}$ . Furthermore, not only are larger particles more porous, but they are less abundant than smaller particles (see section 4.3.1.1). Therefore, when comparing the sinking velocity from different locations in the SSF or LSF, samples with a high fSSF (more abundant small particles) do not necessarily correspond to slower sinking velocities because the composition effect can predominate over the size effect. Indeed, the ratio of 95<sup>th</sup> to 5<sup>th</sup> percentiles is greater for the composition effect than for the size effect in all cruises, demonstrating that there are greater variations in particle density than in particle size distributions.

The hydrography effect generally has lower 95<sup>th</sup> to 5<sup>th</sup> percentile ratios than the size effect. The largest difference between the size and hydrography effects occurs in the western Arctic Ocean, due to a combination of increased variability in size and decreased hydrography effect compared to other oceans.

On a global scale including all three cruises, the concentration effect still leads to most variability in the mass flux in the upper 100 m and the composition effect is the second most important term (Table 1). The high 95<sup>th</sup> to 5<sup>th</sup> percentile ratio for the concentration effect is driven by the very low (5<sup>th</sup> percentile) concentrations in the western Arctic Ocean (Figure 10a-b). The LSF concentration range is more variable than the SSF, whereas the SSF excess density range is more pronounced than the LSF (Table 1). SSF mass flux increases with excess density (Figure 10 b&d). LSF mass flux appears to have little relationship with excess density, until one notices that the GA03 and GP16 data do have a relationship, but the GN01 samples from the western Arctic cluster in a range of relatively high excess density but low mass flux and WSVs (Figure 10 a&c). This is explained by the influence of the significantly smaller particle size distribution and particle concentrations, and most viscous water in the Arctic compared to the North Atlantic and SE Pacific. The relatively similar range ratios between the SSF composition and concentration effects lead to less scatter in the overall relationship of excess density vs. mass flux than the LSF. Additionally, the ratio of 95<sup>th</sup> to 5<sup>th</sup> percentiles for the hydrography effect on a global scale is almost two times higher than that on a regional scale, due to contrasting hydrographic features

842 between polar and tropical oceans (Figure 9), which makes the ratio very similar to the size effect  
 843 (Table 1).

844



845  
 846 Figure 10. Scatter plots between size-fractionated (LSF: left; SSF: right) excess density and mass  
 847 flux in the upper 100 m of all non-shelf stations (bottom depth>200 m). The color bars are  
 848  $\log_{10}(\text{SPM})$  on the top row (a-b), and mass-weighted average sinking velocity (WSVs)  
 849 on the second row (c-d). Note that the y axes and color bar for SPM are in logarithmic scale.  
 850

#### 851 4.3.2.2 Effects on magnitude of mass flux

852 We are also interested in addressing two questions related to the magnitude of mass flux:  
 853 1) why is the magnitude of LSF mass flux smallest in the central basin of western Arctic Ocean?  
 854 2) why do LSF particles dominate the TOT mass flux throughout the water column even though  
 855 they have much smaller mass concentrations than the SSF?

856 First, we assess the difference in magnitudes between four terms in the upper 100 m across  
 857 all cruises. Since the LSF consists of the majority of TOT mass flux, we only discuss LSF flux  
 858 here. The LSF mass flux in the upper 100 m in the western Arctic Ocean is significantly smaller  
 859 than the other two oceans ( $p<<0.001$ ). Indeed, the magnitudes of the concentration and  
 860 hydrography effects are smallest in the western Arctic Ocean (<100 m) ( $p<<0.001$ ), and the size  
 861 effect in the western Arctic Ocean is similar to the SE Pacific ( $p>0.05$ ) but both are smaller than  
 862 the North Atlantic ( $p<0.01$ ). In contrast, the LSF excess density in the western Arctic Ocean is  
 863 significantly larger than the North Atlantic ( $p<0.01$ ) and similar to the SE Pacific ( $p>0.05$ ). The  
 864 slightly higher excess density in the western Arctic Ocean compared to the North Atlantic (median  
 865 excess density in the LSF is 0.7 and 0.5 g/cm³ in the western Arctic Ocean and North Atlantic,  
 866 respectively) cannot compensate for smaller size and hydrography effects, resulting in the smallest

867 LSF WSVs in the upper 100m in the western Arctic (median: 37.8 m/d; p<<0.001; Figure 10c).  
 868 The much lower LSF SPM concentrations in the western Arctic Ocean further decrease the mass  
 869 flux (Figure 10a). Therefore, the lowest mass fluxes in the western Arctic Ocean are not due to a  
 870 lack of ballast minerals as proposed by (Honjo et al., 2010), but rather to a combination of smallest  
 871 particle sizes, lowest particle concentrations and most viscous water (lower g/vis). This conclusion  
 872 also holds true for the rest of the water column.

873 Secondly, high values of mass flux for LSF compared to SSF result from their much higher  
 874 sinking velocities than the SSF (Eq. 13). Indeed, we can determine quantitatively which term (size,  
 875 composition or hydrography) is the main driver elevating sinking velocity over the entire water  
 876 column. Based on our definition of size effect, the ratios of size effect between LSF and SSF can

877 be calculated as:  $\frac{\int_{51}^{5000} \frac{m_i}{\int_{51}^{5000} m_i dd} \times (1-P_i) \times (d_i/10^6)^2 dd}{\int_1^{51} \frac{m_i}{\int_1^{51} m_i dd} \times (1-P_i) \times (d_i/10^6)^2 dd}$ , which is relatively constant, ~41. Given that the ratio

878 of the concentration effect between LSF and SSF over all cruises has a median (5<sup>th</sup>-95<sup>th</sup> percentile  
 879 range) of 0.3 (0.1-0.8), the size alone can more than compensate for lower concentrations in the  
 880 LSF and lead to higher mass flux. Additionally, the LSF excess densities are slightly higher than  
 881 the SSF in the upper 100 m (Figure 10): the median (5<sup>th</sup>-95<sup>th</sup>) ratio of the composition effect  
 882 between LSF and SSF is 1.8 (0.7-4.8). Since both size fractions experience the same hydrographic  
 883 parameters, it is the larger particle sizes and, to a lesser degree, denser particles in the LSF that  
 884 explain the dominance of this size fraction's contribution to the total mass flux.

#### 885 4.3.2.3 Overall dependency of mass flux on particle size

886 Since  $m_i$ ,  $P_i$  and  $W_i$  are functions of  $d_i$  in Eq. 14, we can further substitute Eqs. 2 and 8  
 887 into 14 and derive the overall dependency of  $F$  on  $d_i$ :

$$888 F = 3.6 \times 10^{-14.4} \times \frac{p \times \Delta Q \times g}{18\eta} \times \int_{d_1}^{d_2} (d_i)^{0.8-q} dd \quad (15)$$

889 The integrated mass flux  $F$  is calculated using the mass flux spectrum integrated over a size  
 890 interval  $[d_1, d_2]$ . We simplify Eq. 15 and define the mass flux as  $F = \int_{d_1}^{d_2} f(d) dd$ . The mass flux  
 891 spectrum  $f(d)$  is a power function with positive coefficients and an exponent of 0.8-q. For any  
 892 given particle size, the values of  $f(d)$  are always positive, which leads to positive flux  $F$  for any  
 893 size interval.

894 The median (5<sup>th</sup>-95<sup>th</sup>) of mass-size spectra power  $q$  over all three cruises is 1.4 (1.1-1.6).  
 895 Accordingly, the power of  $f(d)$  has a median (5<sup>th</sup> to 95<sup>th</sup>) of -0.6 (-0.8 to -0.3). Therefore, the mass  
 896 flux spectrum generally has a negative slope, and the function  $f(d)$  decreases with size. The  
 897 negative sign of the power signifies that the mass flux in any single size bin generally decreases  
 898 as a function of particle size, similar to the mass-size and number-size spectra, although the  
 899 absolute magnitude of the power in the mass flux spectrum is much smaller. Noticeably, in some  
 900 rare cases, the mass flux spectrum can even have a positive slope and increase with size. Over the  
 901 Chukchi Shelf in the western Arctic Ocean, there are very low  $q$  values (denoted larger particles),  
 902 reaching as low as 0.6 (Figure S5), which leads to a positive exponent 0.2 in  $f(d)$ .

#### 903 4.4 Key assumptions and their limitations

904 This study relies on several key assumptions: (1) the mass concentration and size follow a  
 905 power-law relationship; (2) a power function also describes the relationship between porosity and

size; (3) the particle composition is the same across the size spectrum within each size fraction for a specific sample; (4) the sinking of particles obeys Stokes' Law. We examine each of these assumptions.

First, due to the difficulties of observing individual particle mass directly, there is not much direct evidence for the application of a single power-law relationship between mass concentration and size. The mass size distribution in this study was derived from bulk measurements of particle mass in two size fractions. Its power law form assumes that the higher abundance of small particles, as confirmed by numerous optical observations of the number size spectrum (e.g., Jackson et al., 1997; Loisel et al., 2006; Roullier et al., 2014; Stemmann et al., 2008; Stemmann et al., 2004), overcomes the greater mass for individual large aggregates, giving rise to a negative slope between the mass concentration and size. Indeed, our data confirm that the mass of particles in the SSF is almost always larger than in the LSF. Applying a single slope to the entire size range is likely an oversimplification for the complex natural assemblage of particles, but hopefully captures the first order distribution of mass.

Secondly, the single power-law function between the porosity and size used in this work is also a simplification of the myriad controls on porosity. Compared to the original equation in Alldredge and Gotschalk (1988), the updated power law in this study incorporates more data points, especially in the smaller end of the size range, as well as different methods for estimating particle porosities. As discussed above in section 4.1, the derived mass flux is quite sensitive to the choice of porosity-size relationship. More data points are needed in future studies, especially in size range of 0.3 to 1.0 mm (Figure 2). It is clear from the considerable scatter in both the original and updated relationships that there are many more controls on porosity than size alone. Given the many mechanisms that produce marine aggregates, including abiotic coagulation and fecal pellet production by a wide variety of animals, it is probable that better estimates of mass fluxes require multiple power functions or a more complicated non-linear relationship.

Thirdly, different particle types (Andrews et al., 2010; Reynolds et al., 2016; Woźniak et al., 2010), and phytoplankton communities (Green et al., 2003a; Green et al., 2003b; Smyth et al., 2019; Stramski et al., 2001) have distinct size distributions, and their corresponding peaks in particle number concentrations do not often occur at the same size. For example, relatively dense lithogenic particles and CaCO<sub>3</sub> coccoliths are likely concentrated in the smaller end of the SSF spectrum (e.g., Baumann & Sprengel, 2000; Rea & Hovan, 1995) rather than distributed evenly throughout. Thus, the assumption of constant composition in all size bins within each size fraction necessarily results in monotonic changes in sinking velocity with size in the LSF or SSF that might not exist in reality. Using an average bulk composition would lead to an overestimate of true mass flux if denser particle phases were skewed to smaller particles. Since measuring particle composition at each size bin is not practical due to sampling and analytical limitations, we apply two different densities to the size range within the LSF and SSF, respectively, to estimate the mass flux. A similar strategy using a single bulk composition was employed by Bach et al. (2016) when calculating the sinking velocity of natural marine aggregates in mesocosms.

Fourthly, the assumption of spherical particles for our Stokes' Law calculations is a simplification, as marine aggregates are not perfect spheres (e.g., Alldredge & Gotschalk, 1988; Engel et al., 2009; McDonnell & Buesseler, 2010). Given the same size and excess density, irregularly shaped aggregates are characterized by lower sinking velocities than spherical ones due to the increased drag (Alldredge & Gotschalk, 1988). Another assumption we made in Stokes' Law calculation is that the flow through the porous aggregate is negligible in order to apply Eq.4. The numerical simulations from Kiørboe et al. (2001), however, suggested that flow occurs in a

thin layer at the surface of aggregates, which is borne out by oxygen microsensor measurements within aggregates (Ploug et al., 2008b). Additionally, the presence of TEP can also influence the excess density in sinking velocity estimations. Indeed, much of the space in the porous fraction of aggregates can be occupied by TEP (Ploug & Passow, 2007). TEP is operationally defined as >0.4 µm particles filtered by polycarbonate filters that stain with Alcian Blue (Alldredge et al., 1993; Passow, 2002). The density of TEP is 0.70-0.84 g/cm<sup>3</sup>, lower than seawater (Azetsu-Scott & Passow, 2004). As TEP measurements were not made in our samples, we did not consider its possible influence, but it would be expected to decrease the mass flux estimation.

## 5. Conclusions

Although this study makes several assumptions to convert suspended particle concentration and composition to mass flux, it predicts mass flux values comparable to various sediment traps studies and gives insights into the controls of export flux on a global scale.

We compile porosity and size measurements of natural marine aggregates from the literature and use a modified Stokes' law with the fractal-porosity relationship to calculate sinking velocity and mass flux. Noticeably, TOT mass fluxes derived from the newly compiled porosity-size power-law relationship are more similar to sediment trap observations than if we were to use the porosity-size relationship for marine snow aggregates only from Alldredge and Gotschalk (1988). The western Arctic Ocean is characterized by the lowest TOT WSVs and mass fluxes compared to the North Atlantic and SE Pacific. We did not find evidence for a lack of ballast minerals in the western Arctic Ocean as proposed by Honjo et al. (2010) to explain low mass fluxes. Instead, the lowest TOT mass fluxes found in the western Arctic Ocean result from the smallest particle sizes, the lowest particle concentrations and the most viscous water. It does not mean that composition is not important in determining the magnitude of mass flux, but simply that other factors dominate in the western Arctic. Indeed, away from the Arctic, the LSF mass flux generally increases with excess density (Figure 10), though there is no relationship with the prevalence of any specific particle phase (Figure S9).

We also compare the relative importance of particle concentration, composition, size and hydrography effects in the variability and magnitude of mass flux on a global scale combining all three cruises. Our data suggest that the variability of mass flux within each size fraction (LSF, SSF or TOT) is controlled mostly by particle concentration and composition, and less so by size and hydrography (Table 1). While large particles will always have a faster sinking velocity than small particles (all else being equal) and thus explain the important contributions of the LSF to the TOT mass flux, the variations in particle size distribution between samples are smaller than the variations in particle density. This highlights the importance of particle composition, not just size distribution, as key parameters for predicting mass flux.

The particle size distribution is a parameter measured by optical methods that is increasingly used to study the biological carbon pump in various cruises and autonomous platforms (Picheral et al., 2017), including the *Tara* Ocean expedition (Guidi et al., 2016). The conversion from particle size to flux, however, often lacks any direct or indirect information about particle composition (Giering et al., 2020; Stemmann & Boss, 2012). The poor constraints in particle densities might partly explain the discrepancy between sediment trap-measured and UVP-derived mass fluxes (Fender et al., 2019; Guidi et al., 2008). Compared to traditional geochemistry measurements, however, optical devices such as the UVP have advantages of much higher spatial and temporal resolution. To better constrain UVP-derived mass flux estimates, we recommend pairing optics with measurements of particle composition in future investigations, either by

999 sampling simultaneously in the same cruise, or referring to historical measurements. The  
1000 geochemical determination of particle properties serves as a calibration to optical proxies, and  
1001 helps us further understand the biological carbon pump on a global scale.

1002

### 1003 Acknowledgments

1004 This work was supported by NSFOCE-1535854 to PJL. We would like to thank all chief scientists  
1005 and everyone on board in the GA03, GP16, and GN01 U.S. GEOTRACES cruises. Special thanks  
1006 to all people in the pump group for helping to collect particle samples at sea. We sincerely thank  
1007 past and current members in the Lam lab for the continuous assistance in both lab work and data  
1008 analysis, and Thomas Weber and Bo Yang for their help in data visualization. We also thank X  
1009 anonymous reviewers for their suggestions and comments to improve this manuscript. All size-  
1010 fractionated particle concentration and composition data described above are available on the  
1011 Biological and Chemical Oceanography Data Management Office website (GA03:  
1012 <https://www.bco-dmo.org/dataset/3871>; GP16: <https://www.bco-dmo.org/dataset/668083>; GN01:  
1013 <https://www.bco-dmo.org/dataset/807340>).

1014

### 1015 References

- 1016 Alldredge, A. L., Cowles, T. J., MacIntyre, S., Rines, J. E. B., Donaghay, P. L., Greenlaw, C.  
1017 F., et al. (2002). Occurrence and mechanisms of formation of a dramatic thin layer of marine  
1018 snow in a shallow Pacific fjord. *Marine Ecology Progress Series*, 233, 1-12.  
1019 doi:10.3354/meps233001
- 1020 Alldredge, A. L., & Crocker, K. M. (1995). Why do sinking mucilage aggregates accumulate  
1021 in the water column? *Science of The Total Environment*, 165(1), 15-22. doi:10.1016/0048-  
1022 9697(95)04539-D
- 1023 Alldredge, A. L., & Gotschalk, C. (1988). In situ settling behavior of marine snow. *Limnology*  
1024 and *Oceanography*, 33(3), 339-351. doi:10.4319/lo.1988.33.3.0339
- 1025 Alldredge, A. L., Passow, U., & Logan, B. E. (1993). The abundance and significance of a  
1026 class of large, transparent organic particles in the ocean. *Deep Sea Research Part I:*  
1027 *Oceanographic Research Papers*, 40(6), 1131-1140. doi:10.1016/0967-0637(93)90129-Q
- 1028 Alldredge, A. L., & Silver, M. W. (1988). Characteristics, dynamics and significance of  
1029 marine snow. *Progress in oceanography*, 20(1), 41-82. doi:10.1016/0079-6611(88)90053-5
- 1030 Alonso-González, I. J., Arístegui, J., Lee, C., Sanchez-Vidal, A., Calafat, A., Fabrés, J., et al.  
1031 (2010). Role of slowly settling particles in the ocean carbon cycle. *Geophysical Research*  
1032 *Letters*, 37(13). doi:10.1029/2010gl043827
- 1033 Anderson, R. F., & Fleisher, M. Q. (2013). Particle beam attenuation coefficient (Cp) data  
1034 from ODF (Ocean Data Facility) rosette, R/V Knorr KN199-04, KN204-01 in the Subtropical  
1035 northern Atlantic Ocean, 2010-2011 (U.S. GEOTRACES NAT project). *Biological and*  
1036 *Chemical Oceanography Data Management Office (BCO-DMO)*, Dataset version 2013-11-05.
- 1037 Andrews, S., Nover, D., & Schladow, S. G. (2010). Using laser diffraction data to obtain  
1038 accurate particle size distributions: the role of particle composition. *Limnology and*  
1039 *Oceanography: Methods*, 8(10), 507-526. doi:10.4319/lom.2010.8.507
- 1040 Armstrong, R. A., Lee, C., Hedges, J. I., Honjo, S., & Wakeham, S. G. (2001). A new,  
1041 mechanistic model for organic carbon fluxes in the ocean based on the quantitative association of  
1042 POC with ballast minerals. *Deep Sea Research Part II: Topical Studies in Oceanography*, 49(1-  
1043 3), 219-236. doi:10.1016/S0967-0645(01)00101-1

- 1044 Armstrong, R. A., Peterson, M. L., Lee, C., & Wakeham, S. G. (2009). Settling velocity  
1045 spectra and the ballast ratio hypothesis. *Deep Sea Research Part II: Topical Studies in*  
1046 *Oceanography*, 56(18), 1470-1478. doi:10.1016/j.dsr2.2008.11.032
- 1047 Aumont, O., Van Hulten, M., Roy-Barman, M., Dutay, J. C., Éthé, C., & Gehlen, M. (2017).  
1048 Variable reactivity of particulate organic matter in a global ocean biogeochemical model.  
1049 *Biogeosciences*, 14(9), 2321-2341. doi:10.5194/bg-14-2321-2017
- 1050 Azetsu-Scott, K., & Passow, U. (2004). Ascending marine particles: Significance of  
1051 transparent exopolymer particles (TEP) in the upper ocean. *Limnology and Oceanography*,  
1052 49(3), 741-748. doi:10.4319/lo.2004.49.3.0741
- 1053 Bach, L. T., Boxhammer, T., Larsen, A., Hildebrandt, N., Schulz, K. G., & Riebesell, U.  
1054 (2016). Influence of plankton community structure on the sinking velocity of marine aggregates.  
1055 *Global Biogeochemical Cycles*, 30(8), 1145-1165. doi:10.1002/2016GB005372
- 1056 Bach, L. T., Stange, P., Taucher, J., Achterberg, E. P., Algueró-Muñiz, M., Horn, H., et al.  
1057 (2019). The influence of plankton community structure on sinking velocity and remineralization  
1058 rate of marine aggregates. *Global Biogeochemical Cycles*, 33(8), 971-994.  
1059 doi:10.1029/2019gb006256
- 1060 Bacon, M. P., & Anderson, R. F. (1982). Distribution of thorium isotopes between dissolved  
1061 and particulate forms in the deep sea. *Journal of Geophysical Research: Oceans*, 87(C3), 2045-  
1062 2056. doi:10.1029/JC087iC03p02045
- 1063 Baumann, K. H., & Sprengel, C. (2000). Morphological variations of selected coccolith  
1064 species in a sediment trap north of the Canary Islands. *Journal of Nannoplankton Research*,  
1065 22(3), 185-193.
- 1066 Berelson, W. M. (2001). Particle settling rates increase with depth in the ocean. *Deep Sea  
1067 Research Part II: Topical Studies in Oceanography*, 49(1-3), 237-251. doi:10.1016/S0967-  
1068 0645(01)00102-3
- 1069 Berelson, W. M., Haskell II, W. Z., Prokopenko, M., Knapp, A. N., Hammond, D. E., Rollins,  
1070 N., & Capone, D. G. (2015). Biogenic particle flux and benthic remineralization in the Eastern  
1071 Tropical South Pacific. *Deep Sea Research Part I: Oceanographic Research Papers*, 99, 23-34.  
1072 doi:10.1016/j.dsr.2014.12.006
- 1073 Bishop, J. K. B., Edmond, J. M., Ketten, D. R., Bacon, M. P., & Silker, W. B. (1977). The  
1074 chemistry, biology, and vertical flux of particulate matter from the upper 400 m of the equatorial  
1075 Atlantic Ocean. *Deep Sea Research*, 24(6), 511-548. doi:10.1016/0146-6291(77)90526-4
- 1076 Bopp, L., Resplandy, L., Orr, J. C., Doney, S. C., Dunne, J. P., Gehlen, M., et al. (2013).  
1077 Multiple stressors of ocean ecosystems in the 21st century: projections with CMIP5 models.  
1078 *Biogeosciences*, 10(10), 6225-6245. doi:10.5194/bg-10-6225-2013
- 1079 Boyd, P. W., & Trull, T. W. (2007). Understanding the export of biogenic particles in oceanic  
1080 waters: Is there consensus? *Progress in Oceanography*, 72(4), 276-312.  
1081 doi:10.1016/j.pocean.2006.10.007
- 1082 Briggs, N., Dall'Olmo, G., & Claustre, H. (2020). Major role of particle fragmentation in  
1083 regulating biological sequestration of CO<sub>2</sub> by the oceans. *Science*, 367(6479), 791-793.  
1084 doi:10.1126/science.aay1790
- 1085 Buesseler, K. O., Lamborg, C. H., Boyd, P. W., Lam, P. J., Trull, T. W., Bidigare, R. R., et al.  
1086 (2007). Revisiting carbon flux through the ocean's twilight zone. *Science*, 316(5824), 567-570.  
1087 doi:10.1126/science.1137959

- 1088 Burd, A. B., Jackson, G. A., & Moran, S. B. (2007). The role of the particle size spectrum in  
1089 estimating POC fluxes from Th234/U238 disequilibrium. *Deep Sea Research Part I: Oceanographic Research Papers*, 54(6), 897-918. doi:10.1016/j.dsr.2007.03.006
- 1090 Cavan, E. L., Henson, S. A., & Boyd, P. W. (2019). The sensitivity of subsurface microbes to  
1091 ocean warming accentuates future declines in particulate carbon export. *Frontiers in Ecology and Evolution*, 6, 230. doi:10.3389/fevo.2018.00230
- 1092 Cutter, G., Kadko, D., & Landing, W. M. (2019). Bottle data from the CTD-ODF carousel on  
1093 the GEOTRACES Arctic Section cruise (HY1502) from August to October 2015 (U.S. GEOTRACES Arctic project). *Biological and Chemical Oceanography Data Management Office (BCO-DMO)*, Dataset version 2019-07-29. doi:10.1575/1912/bco-dmo.646825.4
- 1094 De La Rocha, C. L., Nowald, N., & Passow, U. (2008). Interactions between diatom  
1095 aggregates, minerals, particulate organic carbon, and dissolved organic matter: Further  
1096 implications for the ballast hypothesis. *Global Biogeochemical Cycles*, 22(4).  
1097 doi:10.1029/2007gb003156
- 1098 Ebersbach, F., & Trull, T. W. (2008). Sinking particle properties from polyacrylamide gels  
1099 during the Kerguelan Ocean and Plateau compared Study (KEOPS): Zooplankton control of  
1100 carbon export in an area of persistent natural iron inputs in the Southern Ocean. *Limnology and  
1101 Oceanography*, 53(1), 212-224. doi:10.4319/lo.2008.53.1.0212
- 1102 Engel, A., Szlosek, J., Abramson, L., Liu, Z., & Lee, C. (2009). Investigating the effect of  
1103 ballasting by CaCO<sub>3</sub> in Emiliania huxleyi: I. Formation, settling velocities and physical  
1104 properties of aggregates. *Deep Sea Research Part II: Topical Studies in Oceanography*, 56(18),  
1105 1396-1407. doi:10.1016/j.dsr2.2008.11.027
- 1106 Estapa, M. L., Feen, M. L., & Breves, E. (2019). Direct observations of biological carbon  
1107 export from profiling floats in the subtropical North Atlantic. *Global Biogeochemical Cycles*,  
1108 33(3), 282-300. doi:10.1029/2018gb006098
- 1109 Fender, C. K., Kelly, T. B., Guidi, L., Ohman, M. D., Smith, M. C., & Stukel, M. R. (2019).  
1110 Investigating particle size-flux relationships and the biological pump across a range of plankton  
1111 ecosystem states from coastal to oligotrophic. *Frontiers in Marine Science*, 6(603).  
1112 doi:10.3389/fmars.2019.00603
- 1113 Fowler, S. W., & Knauer, G. A. (1986). Role of large particles in the transport of elements  
1114 and organic compounds through the oceanic water column. *Progress in oceanography*, 16(3),  
1115 147-194. doi:10.1016/0079-6611(86)90032-7
- 1116 Francois, R., Honjo, S., Krishfield, R., & Manganini, S. (2002). Factors controlling the flux of  
1117 organic carbon to the bathypelagic zone of the ocean. *Global Biogeochemical Cycles*, 16(4), 34-  
1118 31-34-20. doi:10.1029/2001gb001722
- 1119 Gardner, W. D., Mishonov, A. V., & Richardson, M. J. (2018a). Decadal comparisons of  
1120 particulate matter in repeat transects in the Atlantic, Pacific, and Indian Ocean Basins.  
1121 *Geophysical Research Letters*, 45(1), 277-286. doi:10.1002/2017GL076571
- 1122 Gardner, W. D., Richardson, M. J., & Mishonov, A. V. (2018b). Global assessment of benthic  
1123 nepheloid layers and linkage with upper ocean dynamics. *Earth and Planetary Science Letters*,  
1124 482, 126-134. doi:10.1016/j.epsl.2017.11.008
- 1125 Gardner, W. D., Richardson, M. J., Mishonov, A. V., & Biscaye, P. E. (2018c). Global  
1126 comparison of benthic nepheloid layers based on 52 years of nephelometer and transmissometer  
1127 measurements. *Progress in oceanography*, 168, 100-111. doi:10.1016/j.pocean.2018.09.008

- 1132 Giering, S. L. C., Cavan, E. L., Basedow, S. L., Briggs, N., Burd, A. B., Darroch, L. J., et al.  
1133 (2020). Sinking organic particles in the ocean- flux estimates from in situ optical devices.  
1134 *Frontiers in Marine Science*, 6(834). doi:10.3389/fmars.2019.00834
- 1135 Giering, S. L. C., Sanders, R., Martin, A. P., Lindemann, C., Möller, K. O., Daniels, C. J., et  
1136 al. (2016). High export via small particles before the onset of the North Atlantic spring bloom.  
1137 *Journal of Geophysical Research: Oceans*, 121(9), 6929-6945. doi:10.1002/2016jc012048
- 1138 Green, R. E., Sosik, H. M., & Olson, R. J. (2003a). Contributions of phytoplankton and other  
1139 particles to inherent optical properties in New England continental shelf waters. *Limnology and*  
1140 *Oceanography*, 46(6), 2377-2391. doi:10.4319/lo.2003.46.6.2377
- 1141 Green, R. E., Sosik, H. M., Olson, R. J., & DuRand, M. D. (2003b). Flow cytometric  
1142 determination of size and complex refractive index for marine particles: comparison with  
1143 independent and bulk estimates. *Applied Optics*, 42(3), 526-541. doi:10.1364/AO.42.000526
- 1144 Guidi, L., Chaffron, S., Bittner, L., Eveillard, D., Larhlimi, A., Roux, S., et al. (2016).  
1145 Plankton networks driving carbon export in the oligotrophic ocean. *Nature*, 532(7600), 465-470.  
1146 doi:10.1038/nature16942
- 1147 Guidi, L., Jackson, G. A., Stemmann, L., Miquel, J. C., Picheral, M., & Gorsky, G. (2008).  
1148 Relationship between particle size distribution and flux in the mesopelagic zone. *Deep Sea*  
1149 *Research Part I: Oceanographic Research Papers*, 55(10), 1364-1374.  
1150 doi:10.1016/j.dsr.2008.05.014
- 1151 Gustafsson, Ö., Andersson, P., Roos, P., Kukulska, Z., Broman, D., Larsson, U., et al. (2004).  
1152 Evaluation of the collection efficiency of upper ocean sub-photoc-layer sediment traps: A 24-  
1153 month in situ calibration in the open Baltic Sea using  $^{234}\text{Th}$ . *Limnology and Oceanography:*  
1154 *Methods*, 2(2), 62-74. doi:10.4319/lom.2004.2.62
- 1155 Hamm, C. E. (2002). Interactive aggregation and sedimentation of diatoms and clay-sized  
1156 lithogenic material. *Limnology and Oceanography*, 47(6), 1790-1795.  
1157 doi:10.4319/lo.2002.47.6.1790
- 1158 Hatta, M., Measures, C. I., Wu, J., Roshan, S., Fitzsimmons, J. N., Sedwick, P. N., & Morton,  
1159 P. L. (2015). An overview of dissolved Fe and Mn distributions during the 2010–2011 US  
1160 GEOTRACES north Atlantic cruises: GEOTRACES GA03. *Deep Sea Research Part II: Topical*  
1161 *Studies in Oceanography*, 116, 117-129. doi:10.1016/j.dsr2.2014.07.005
- 1162 Henson, S. A., Sanders, R., & Madsen, E. (2012). Global patterns in efficiency of particulate  
1163 organic carbon export and transfer to the deep ocean. *Global Biogeochemical Cycles*, 26(1).  
1164 doi:10.1029/2011gb004099
- 1165 Honjo, S., Dymond, J., Collier, R., & Manganini, S. J. (1995). Export production of particles  
1166 to the interior of the equatorial Pacific Ocean during the 1992 EqPac experiment. *Deep Sea*  
1167 *Research Part II: Topical Studies in Oceanography*, 42(2-3), 831-870. doi:10.1016/0967-  
1168 0645(95)00034-N
- 1169 Honjo, S., Krishfield, R. A., Eglinton, T. I., Manganini, S. J., Kemp, J. N., Doherty, K., et al.  
1170 (2010). Biological pump processes in the cryopelagic and hemipelagic Arctic Ocean: Canada  
1171 Basin and Chukchi Rise. *Progress in Oceanography*, 85(3-4), 137-170.  
1172 doi:10.1016/j.pocean.2010.02.009
- 1173 Hurd, D. C., & Theyer, F. (1977). Changes in the physical and chemical properties of  
1174 biogenic silica from the central equatorial Pacific; Part II, Refractive index, density, and water  
1175 content of acid-cleaned samples. *American Journal of Science*, 277(9), 1168-1202.  
1176 doi:10.2475/ajs.277.9.1168

- 1177 Hwang, J., Kim, M., Manganini, S. J., McIntyre, C. P., Haghipour, N., Park, J., et al. (2015).  
1178 Temporal and spatial variability of particle transport in the deep Arctic Canada Basin. *Journal of*  
1179 *Geophysical Research: Oceans*, 120(4), 2784-2799. doi:10.1002/2014jc010643
- 1180 Iversen, M. H., & Ploug, H. (2010). Ballast minerals and the sinking carbon flux in the ocean:  
1181 carbon-specific respiration rates and sinking velocity of marine snow aggregates.  
1182 *Biogeosciences*, 7(9), 2613-2624. doi:10.5194/bg-7-2613-2010
- 1183 Iversen, M. H., & Robert, M. L. (2015). Ballasting effects of smectite on aggregate formation  
1184 and export from a natural plankton community. *Marine Chemistry*, 175, 18-27.  
1185 doi:10.1016/j.marchem.2015.04.009
- 1186 Jackson, G. A., Maffione, R., Costello, D. K., Alldredge, A. L., Logan, B. E., & Dam, H. G.  
1187 (1997). Particle size spectra between 1  $\mu\text{m}$  and 1 cm at Monterey Bay determined using multiple  
1188 instruments. *Deep Sea Research Part I: Oceanographic Research Papers*, 44(11), 1739-1767.  
1189 doi:10.1016/S0967-0637(97)00029-0
- 1190 Jakobsson, M. (2002). Hypsometry and volume of the Arctic Ocean and its constituent seas.  
1191 *Geochemistry, Geophysics, Geosystems*, 3(5), 1-18. doi:10.1029/2001GC000302
- 1192 Jenkinson, I. R. (1986). Oceanographic implications of non-newtonian properties found in  
1193 phytoplankton cultures. *Nature*, 323(6087), 435-437. doi:10.1038/323435a0
- 1194 Jenkinson, I. R. (1993). Bulk-phase viscoelastic properties of seawater. *Oceanol. acta*, 16(4),  
1195 317-334.
- 1196 Jenkinson, I. R., & Biddanda, B. A. (1995). Bulk-phase viscoelastic properties of seawater  
1197 relationship with plankton components. *Journal of Plankton Research*, 17(12), 2251-2274.  
1198 doi:10.1093/plankt/17.12.2251
- 1199 Kindler, K., Khalili, A., & Stocker, R. (2010). Diffusion-limited retention of porous particles  
1200 at density interfaces. *Proceedings of the National Academy of Sciences*, 107(51), 22163-22168.  
1201 doi:10.1073/pnas.1012319108
- 1202 Kiørboe, T., Ploug, H., & Thygesen, U. H. (2001). Fluid motion and solute distribution  
1203 around sinking aggregates. I. Small-scale fluxes and heterogeneity of nutrients in the pelagic  
1204 environment. *Marine Ecology Progress Series*, 211, 1-13. doi:10.3354/meps211001
- 1205 Kipp, L. E., Sanial, V., Henderson, P. B., van Beek, P., Reyss, J. L., Hammond, D. E., et al.  
1206 (2018). Radium isotopes as tracers of hydrothermal inputs and neutrally buoyant plume  
1207 dynamics in the deep ocean. *Marine Chemistry*, 201, 51-65. doi:10.1016/j.marchem.2017.06.011
- 1208 Klaas, C., & Archer, D. E. (2002). Association of sinking organic matter with various types of  
1209 mineral ballast in the deep sea: Implications for the rain ratio. *Global Biogeochemical Cycles*,  
1210 16(4), 63-61-63-14. doi:10.1029/2001GB001765
- 1211 Krishnaswami, S., Sarin, M. M., & Somayajulu, B. L. K. (1981). Chemical and radiochemical  
1212 investigations of surface and deep particles of the Indian Ocean. *Earth and Planetary Science  
1213 Letters*, 54(1), 81-96. doi:10.1016/0012-821X(81)90071-6
- 1214 Kwon, E. Y., Primeau, F., & Sarmiento, J. L. (2009). The impact of remineralization depth on  
1215 the air-sea carbon balance. *Nature Geoscience*, 2(9), 630-635. doi:10.1038/ngeo612
- 1216 Lam, P. J., & Bishop, J. K. B. (2007). High biomass, low export regimes in the Southern  
1217 Ocean. *Deep Sea Research Part II: Topical Studies in Oceanography*, 54(5-7), 601-638.  
1218 doi:10.1016/j.dsr2.2007.01.013
- 1219 Lam, P. J., Doney, S. C., & Bishop, J. K. B. (2011). The dynamic ocean biological pump:  
1220 Insights from a global compilation of particulate organic carbon, CaCO<sub>3</sub>, and opal concentration  
1221 profiles from the mesopelagic. *Global Biogeochemical Cycles*, 25(3).  
1222 doi:10.1029/2010gb003868

- 1223 Lam, P. J., Lee, J. M., Heller, M. I., Mehic, S., Xiang, Y., & Bates, N. R. (2018). Size-  
1224 fractionated distributions of suspended particle concentration and major phase composition from  
1225 the US GEOTRACES Eastern Pacific Zonal Transect (GP16). *Marine Chemistry*, 201, 90-107.  
1226 doi:10.1016/j.marchem.2017.08.013
- 1227 Lam, P. J., & Marchal, O. (2015). Insights into particle cycling from thorium and particle  
1228 data. *Annual review of marine science*, 7, 159-184. doi:10.1146/annurev-marine-010814-015623
- 1229 Lam, P. J., Ohnemus, D. C., & Auro, M. E. (2015). Size-fractionated major particle  
1230 composition and concentrations from the US GEOTRACES North Atlantic Zonal Transect. *Deep  
1231 Sea Research Part II: Topical Studies in Oceanography*, 116, 303-320.  
1232 doi:10.1016/j.dsr2.2014.11.020
- 1233 Laufkötter, C., Vogt, M., Gruber, N., Aumont, O., Bopp, L., Doney, S. C., et al. (2016).  
1234 Projected decreases in future marine export production: the role of the carbon flux through the  
1235 upper ocean ecosystem. *Biogeosciences*, 13(13), 4023-4047. doi:10.5194/bg-13-4023-2016
- 1236 Laurenceau-Cornec, E. C., Le Moigne, F. A. C., Gallinari, M., Moriceau, B., Toullec, J.,  
1237 Iversen, M. H., et al. (2020). New guidelines for the application of Stokes' models to the sinking  
1238 velocity of marine aggregates. *Limnology and Oceanography*, 65(6), 1264-1285.  
1239 doi:10.1002/lo.11388
- 1240 Laurenceau-Cornec, E. C., Trull, T. W., Davies, D. M., Bray, S. G., Doran, J., Planchon, F., et  
1241 al. (2015a). The relative importance of phytoplankton aggregates and zooplankton fecal pellets to  
1242 carbon export: insights from free-drifting sediment trap deployments in naturally iron-fertilised  
1243 waters near the Kerguelen Plateau. *Biogeosciences*, 12(4), 1007-1027. doi:10.5194/bg-12-1007-  
1244 2015
- 1245 Laurenceau-Cornec, E. C., Trull, T. W., Davies, D. M., Christina, L., & Blain, S. (2015b).  
1246 Phytoplankton morphology controls on marine snow sinking velocity. *Marine Ecology Progress Series*  
1247 Series, 520, 35-56. doi:10.3354/meps11116
- 1248 Le Moigne, F. A. C., Sanders, R. J., Villa-Alfageme, M., Martin, A. P., Pabortsava, K.,  
1249 Planquette, H., et al. (2012). On the proportion of ballast versus non-ballast associated carbon  
1250 export in the surface ocean. *Geophysical research letters*, 39(15). doi:10.1029/2012GL052980
- 1251 Lee, C., Peterson, M. L., Wakeham, S. G., Armstrong, R. A., Cochran, J. K., Miquel, J. C., et  
1252 al. (2009). Particulate organic matter and ballast fluxes measured using time-series and settling  
1253 velocity sediment traps in the northwestern Mediterranean Sea. *Deep Sea Research Part II:  
1254 Topical Studies in Oceanography*, 56(18), 1420-1436. doi:10.1016/j.dsr2.2008.11.029
- 1255 Lee, J. M., Heller, M. I., & Lam, P. J. (2018). Size distribution of particulate trace elements in  
1256 the U.S. GEOTRACES Eastern Pacific Zonal Transect (GP16). *Marine Chemistry*, 201, 108-  
1257 123. doi:10.1016/j.marchem.2017.09.006
- 1258 Lerner, P., Marchal, O., Lam, P. J., Buesseler, K., & Charette, M. A. (2017). Kinetics of  
1259 thorium and particle cycling along the U.S. GEOTRACES North Atlantic Transect. *Deep Sea  
1260 Research Part I: Oceanographic Research Papers*, 125, 106-128. doi:10.1016/j.dsr.2017.05.003
- 1261 Lima, I. D., Lam, P. J., & Doney, S. C. (2014). Dynamics of particulate organic carbon flux in  
1262 a global ocean model. *Biogeosciences*, 11(4), 1177-1198. doi:10.5194/bg-11-1177-2014
- 1263 Logan, B. E., & Alldredge, A. L. (1989). Potential for increased nutrient uptake by  
1264 flocculating diatoms. *Marine Biology*, 101(4), 443-450. doi:10.1007/BF00541645
- 1265 Logan, B. E., & Wilkinson, D. B. (1990). Fractal geometry of marine snow and other  
1266 biological aggregates. *Limnology and Oceanography*, 35(1), 130-136.  
1267 doi:10.4319/lo.1990.35.1.0130

- 1268 Loisel, H., Nicolas, J. M., Sciandra, A., Stramski, D., & Poteau, A. (2006). Spectral  
1269 dependency of optical backscattering by marine particles from satellite remote sensing of the  
1270 global ocean. *Journal of Geophysical Research: Oceans*, 111(C9). doi:10.1029/2005JC003367
- 1271 MacIntyre, S., Alldredge, A. L., & Gotschalk, C. C. (1995). Accumulation of marines now at  
1272 density discontinuities in the water column. *Limnology and Oceanography*, 40(3), 449-468.  
1273 doi:10.4319/lo.1995.40.3.0449
- 1274 Mahowald, N. M., Baker, A. R., Bergametti, G., Brooks, N., Duce, R. A., Jickells, T. D., et al.  
1275 (2005). Atmospheric global dust cycle and iron inputs to the ocean. *Global Biogeochemical  
1276 Cycles*, 19(4), n/a-n/a. doi:10.1029/2004gb002402
- 1277 Mandernack, K. W., & Tebo, B. M. (1993). Manganese scavenging and oxidation at  
1278 hydrothermal vents and in vent plumes. *Geochimica et Cosmochimica Acta*, 57(16), 3907-3923.  
1279 doi:10.1016/0016-7037(93)90343-U
- 1280 Marsay, C. M., Kadko, D., Landing, W. M., Morton, P. L., Summers, B. A., & Buck, C. S.  
1281 (2018). Concentrations, provenance and flux of aerosol trace elements during US GEOTRACES  
1282 Western Arctic cruise GN01. *Chemical Geology*, 502, 1-14. doi:10.1016/j.chemgeo.2018.06.007
- 1283 Martin, J. H., Knauer, G. A., Karl, D. M., & Broenkow, W. W. (1987). VERTEX: carbon  
1284 cycling in the northeast Pacific. *Deep Sea Research Part A. Oceanographic Research Papers*,  
1285 34(2), 267-285. doi:10.1016/0198-0149(87)90086-0
- 1286 McDonnell, A. M., & Buesseler, K. O. (2010). Variability in the average sinking velocity of  
1287 marine particles. *Limnology and Oceanography*, 55(5), 2085-2096.  
1288 doi:10.4319/lo.2010.55.5.2085
- 1289 McDonnell, A. M. P., & Buesseler, K. O. (2012). A new method for the estimation of sinking  
1290 particle fluxes from measurements of the particle size distribution, average sinking velocity, and  
1291 carbon content. *Limnology and Oceanography: Methods*, 10(5), 329-346.  
1292 doi:10.4319/lom.2012.10.329
- 1293 Millero, F. J. (1974). Seawater as a multicomponent electrolyte solution. In E. D. Goldberg  
1294 (Eds.), *The Sea, Volume 5: Marine Chemistry* (pp. 3-80): John Wiley & Sons Inc.
- 1295 Nowald, N., Fischer, G., Ratmeyer, V., Iversen, M., Reuter, C., & Wefer, G. (2009). *In-situ  
1296 sinking speed measurements of marine snow aggregates acquired with a settling chamber  
1297 mounted to the Cherokee ROV*. Paper presented at Oceans 2009-Europe, IEEE.
- 1298 Nowald, N., Iversen, M. H., Fischer, G., Ratmeyer, V., & Wefer, G. (2015). Time series of in-  
1299 situ particle properties and sediment trap fluxes in the coastal upwelling filament off Cape Blanc,  
1300 Mauritania. *Progress in Oceanography*, 137, 1-11. doi:10.1016/j.pocean.2014.12.015
- 1301 Omand, M. M., Govindarajan, R., He, J., & Mahadevan, A. (2020). Sinking flux of particulate  
1302 organic matter in the oceans: Sensitivity to particle characteristics. *Scientific reports*, 10(1), 1-16.  
1303 doi:10.1038/s41598-020-60424-5
- 1304 Passow, U. (2002). Transparent exopolymer particles (TEP) in aquatic environments.  
1305 *Progress in Oceanography*, 55(3), 287-333. doi:10.1016/S0079-6611(02)00138-6
- 1306 Passow, U., & De La Rocha, C. L. (2006). Accumulation of mineral ballast on organic  
1307 aggregates. *Global Biogeochemical Cycles*, 20(1). doi:10.1029/2005gb002579
- 1308 Passow, U., De La Rocha, C. L., Fairfield, C., & Schmidt, K. (2014). Aggregation as a  
1309 function of and mineral particles. *Limnology and Oceanography*, 59(2), 532-547.  
1310 doi:10.4319/lo.2014.59.2.0532
- 1311 Pavia, F. J., Anderson, R. F., Lam, P. J., Cael, B. B., Vivancos, S. M., Fleisher, M. Q., et al.  
1312 (2019). Shallow particulate organic carbon regeneration in the South Pacific Ocean. *Proceedings  
1313 of the National Academy of Sciences*, 116(20), 9753-9758. doi:10.1073/pnas.1901863116

- 1314 Peters, B. D., Lam, P. J., & Casciotti, K. L. (2018). Nitrogen and oxygen isotope  
1315 measurements of nitrate along the US GEOTRACES Eastern Pacific Zonal Transect (GP16)  
1316 yield insights into nitrate supply, remineralization, and water mass transport. *Marine Chemistry*,  
1317 201, 137-150. doi:10.1016/j.marchem.2017.09.009
- 1318 Peterson, M. L., Wakeham, S. G., Lee, C., Askea, M. A., & Miquel, J. C. (2005). Novel  
1319 techniques for collection of sinking particles in the ocean and determining their settling rates.  
1320 *Limnology and Oceanography: Methods*, 3(12), 520-532. doi:10.4319/lom.2005.3.520
- 1321 Picheral, M., Colin, S., & Irisson, J. O. (2017). EcoTaxa, a tool for the taxonomic  
1322 classification of images. Available from: <http://ecotaxa.obs-vlfr.fr>
- 1323 Pilskaln, C. H., Lehmann, C., Paduan, J. B., & Silver, M. W. (1998). Spatial and temporal  
1324 dynamics in marine aggregate abundance, sinking rate and flux: Monterey Bay, central  
1325 California. *Deep Sea Research Part II: Topical Studies in Oceanography*, 45(8-9), 1803-1837.  
1326 doi:10.1016/S0967-0645(98)80018-0
- 1327 Ploug, H., Iversen, M. H., & Fischer, G. (2008a). Ballast, sinking velocity, and apparent  
1328 diffusivity within marine snow and zooplankton fecal pellets: Implications for substrate turnover  
1329 by attached bacteria. *Limnology and Oceanography*, 53(5), 1878-1886.  
1330 doi:10.4319/lo.2008.53.5.1878
- 1331 Ploug, H., Iversen, M. H., Koski, M., & Buitenhuis, E. T. (2008b). Production, oxygen  
1332 respiration rates, and sinking velocity of copepod fecal pellets: direct measurements of ballasting  
1333 by opal and calcite. *Limnology and Oceanography*, 53(2), 469-476.  
1334 doi:10.4319/lo.2008.53.2.0469
- 1335 Ploug, H., & Passow, U. (2007). Direct measurement of diffusivity within diatom aggregates  
1336 containing transparent exopolymer particles. *Limnology and oceanography*, 52(1), 1-6.  
1337 doi:10.4319/lo.2007.52.1.0001
- 1338 Prairie, J. C., Ziervogel, K., Arnosti, C., Camassa, R., Falcon, C., Khatri, S., et al. (2013).  
1339 Delayed settling of marine snow at sharp density transitions driven by fluid entrainment and  
1340 diffusion-limited retention. *Marine Ecology Progress Series*, 487, 185-200.  
1341 doi:10.3354/meps10387
- 1342 Prairie, J. C., Ziervogel, K., Camassa, R., McLaughlin, R. M., White, B. L., Dewald, C., &  
1343 Arnosti, C. (2015). Delayed settling of marine snow: Effects of density gradient and particle  
1344 properties and implications for carbon cycling. *Marine Chemistry*, 175, 28-38.  
1345 doi:10.1016/j.marchem.2015.04.006
- 1346 Puigcorbé, V., Benítez-Nelson, C. R., Masqué, P., Verdeny, E., White, A. E., Popp, B. N., et  
1347 al. (2015). Small phytoplankton drive high summertime carbon and nutrient export in the Gulf of  
1348 California and Eastern Tropical North Pacific. *Global Biogeochemical Cycles*, 29(8), 1309-1332.  
1349 doi:10.1002/2015gb005134
- 1350 Rea, D. K., & Hovan, S. A. (1995). Grain size distribution and depositional processes of the  
1351 mineral component of abyssal sediments: Lessons from the North Pacific. *Paleoceanography*,  
1352 10(2), 251-258. doi:10.1029/94PA03355
- 1353 Resing, J. A., Sedwick, P. N., German, C. R., Jenkins, W. J., Moffett, J. W., Sohst, B. M., &  
1354 Tagliabue, A. (2015). Basin-scale transport of hydrothermal dissolved metals across the South  
1355 Pacific Ocean. *Nature*, 523(7559), 200-203. doi:10.1038/nature14577
- 1356 Reynolds, R. A., Stramski, D., & Neukermans, G. (2016). Optical backscattering by particles  
1357 in Arctic seawater and relationships to particle mass concentration, size distribution, and bulk  
1358 composition. *Limnology and Oceanography*, 61(5), 1869-1890. doi:10.1002/lo.10341

- 1359 Riley, J. S., Sanders, R., Marsay, C., Le Moigne, F. A. C., Achterberg, E. P., & Poulton, A. J.  
1360 (2012). The relative contribution of fast and slow sinking particles to ocean carbon export.  
1361 *Global Biogeochemical Cycles*, 26(1), n/a-n/a. doi:10.1029/2011gb004085
- 1362 Rixen, T., Gaye, B., Emeis, K., & Ramaswamy, V. (2019). The ballast effect of lithogenic  
1363 matter and its influences on the carbon fluxes in the Indian Ocean. *Biogeosciences*, 16(2), 485-  
1364 503. doi:10.5194/bg-16-485-2019
- 1365 Rohatgi, A. (2010). WebPlotDigitizer- Extract data from plots, images, and maps. Available  
1366 from: <https://automeris.io/WebPlotDigitizer/>
- 1367 Rosengard, S. Z., Lam, P. J., Balch, W. M., Auro, M. E., Pike, S., Drapeau, D., & Bowler, B.  
1368 (2015). Carbon export and transfer to depth across the Southern Ocean Great Calcite Belt.  
1369 *Biogeosciences*, 12(13), 3953-3971. doi:10.5194/bg-12-3953-2015
- 1370 Roullier, F., Berline, L., Guidi, L., Durrieu De Madron, X., Picheral, M., Sciandra, A., et al.  
1371 (2014). Particle size distribution and estimated carbon flux across the Arabian Sea oxygen  
1372 minimum zone. *Biogeosciences*, 11(16), 4541-4557. doi:10.5194/bg-11-4541-2014
- 1373 Ruiz, J. (1997). What generates daily cycles of marine snow? *Deep Sea Research Part I: Oceanographic Research Papers*, 44(7), 1105-1126. doi:10.1016/S0967-0637(97)00012-5
- 1375 Rutgers van der Loeff, M. M., & Berger, G. W. (1993). Scavenging of 230Th and 231Pa near  
1376 the antarctic polar front in the South Atlantic. *Deep Sea Research Part I: Oceanographic Research Papers*, 40(2), 339-357. doi:10.1016/0967-0637(93)90007-P
- 1378 Santschi, P. H., Murray, J. W., Baskaran, M., Benitez-Nelson, C. R., Guo, L. D., Hung, C. C.,  
1379 et al. (2006). Thorium speciation in seawater. *Marine Chemistry*, 100(3), 250-268.  
1380 doi:10.1016/j.marchem.2005.10.024
- 1381 Schlitzer, R., Anderson, R. F., Dodas, E. M., Lohan, M., Geibert, W., Tagliabue, A., et al.  
1382 (2018). The GEOTRACES intermediate data product 2017. *Chemical Geology*, 493(C), 210-223.  
1383 doi:10.1016/j.chemgeo.2018.05.040
- 1384 Schmidt, K., De La Rocha, C. L., Gallinari, M., & Cortese, G. (2014). Not all calcite ballast is  
1385 created equal: differing effects of foraminiferan and coccolith calcite on the formation and  
1386 sinking of aggregates. *Biogeosciences*, 11(1), 135-145. doi:10.5194/bg-11-135-2014
- 1387 Scholten, J. C., Rutgers van der Loeff, M. M., & Michel, A. (1995). Distribution of 230Th  
1388 and 231Pa in the water column in relation to the ventilation of the deep Arctic basins. *Deep Sea Research Part II: Topical Studies in Oceanography*, 42(6), 1519-1531. doi:10.1016/0967-0645(95)00052-6
- 1391 Seuront, L., Lacheze, C., Doubell, M. J., Seymour, J. R., Van Dongen-Vogels, V., Newton,  
1392 K., et al. (2007). The influence of Phaeocystis globosa on microscale spatial patterns of  
1393 chlorophyll a and bulk-phase seawater viscosity. In M. A. van Leeuwe, J. Stefels, S. Belviso, C.  
1394 Lancelot, P. G. Verity and W. W. C. Gieskes (Eds.), *Phaeocystis, major link in the  
1395 biogeochemical cycling of climate-relevant elements* (pp. 173-188). Dordrecht: Springer  
1396 Netherlands. doi:10.1007/978-1-4020-6214-8\_13
- 1397 Seuront, L., Leterme, S. C., Seymour, J. R., Mitchell, J. G., Ashcroft, D., Noble, W., et al.  
1398 (2010). Role of microbial and phytoplanktonic communities in the control of seawater viscosity  
1399 off East Antarctica (30-80° E). *Deep Sea Research Part II: Topical Studies in Oceanography*,  
1400 57(9), 877-886. doi:10.1016/j.dsr2.2008.09.018
- 1401 Seuront, L., & Vincent, D. (2008). Increased seawater viscosity, Phaeocystis globosa spring  
1402 bloom and Temora longicornis feeding and swimming behaviours. *Marine Ecology Progress Series*,  
1403 363, 131-145. doi:10.3354/meps07373

- 1404 Seuront, L., Vincent, D., & Mitchell, J. G. (2006). Biologically induced modification of  
1405 seawater viscosity in the Eastern English Channel during a *Phaeocystis globosa* spring bloom.  
1406 *Journal of Marine Systems*, 61(3), 118-133. doi:10.1016/j.jmarsys.2005.04.010
- 1407 Shanks, A. L., & Trent, J. D. (1980). Marine snow: sinking rates and potential role in vertical  
1408 flux. *Deep Sea Research Part A. Oceanographic Research Papers*, 27(2), 137-143.  
1409 doi:10.1016/0198-0149(80)90092-8
- 1410 Smyth, T. J., Tarran, G. A., & Sathyendranath, S. (2019). Marine picoplankton size  
1411 distribution and optical property contrasts throughout the Atlantic Ocean revealed using flow  
1412 cytometry. *Applied Optics*, 58(32), 8802-8815. doi:10.1364/AO.58.008802
- 1413 Stemmann, L., & Boss, E. (2012). Plankton and particle size and packaging: from determining  
1414 optical properties to driving the biological pump. *Annual Review of Marine Science*, 4, 263-290.  
1415 doi:10.1146/annurev-marine-120710-100853
- 1416 Stemmann, L., Eloire, D., Sciandra, A., Jackson, G. A., Guidi, L., Picheral, M., & Gorsky, G.  
1417 (2008). Volume distribution for particles between 3.5 to 2000  $\mu\text{m}$  in the upper 200 m region of  
1418 the South Pacific Gyre. *Biogeosciences*, 5(2), 299-310. doi:10.5194/bg-5-299-2008
- 1419 Stemmann, L., Jackson, G. A., & Ianson, D. (2004). A vertical model of particle size  
1420 distributions and fluxes in the midwater column that includes biological and physical  
1421 processes—Part I: model formulation. *Deep Sea Research Part I: Oceanographic Research  
1422 Papers*, 51(7), 865-884. doi:10.1016/j.dsr.2004.03.001
- 1423 Stokes, G. G. (1851). On the effect of the internal friction of fluids on the motion of  
1424 pendulums. *Transactions of the Cambridge Philosophical Society*, 9, 8-106.
- 1425 Stramski, D., Bricaud, A., & Morel, A. (2001). Modeling the inherent optical properties of the  
1426 ocean based on the detailed composition of the planktonic community. *Applied Optics*, 40(18),  
1427 2929-2945. doi:10.1364/AO.40.002929
- 1428 Thyng, K. M., Greene, C. A., Hetland, R. D., Zimmerle, H. M., & DiMarco, S. F. (2016).  
1429 True colors of oceanography: Guidelines for effective and accurate colormap selection.  
1430 *Oceanography*, 29(3), 9-13. doi:10.5670/oceanog.2016.66
- 1431 Torres-Valdés, S., Painter, S. C., Martin, A. P., Sanders, R., & Felden, J. (2014). Data  
1432 compilation of fluxes of sedimenting material from sediment traps in the Atlantic Ocean. *Earth  
1433 System Science Data*, 6(1), 123-145. doi:10.5194/essd-6-123-2014
- 1434 Towe, K. M., & Bradley, W. F. (1967). Mineralogical constitution of colloidal “hydrous ferric  
1435 oxides”. *Journal of Colloid and Interface Science*, 24(3), 384-392. doi:10.1016/0021-  
1436 9797(67)90266-4
- 1437 Trull, T. W., Bray, S. G., Buesseler, K. O., Lamborg, C. H., Manganini, S., Moy, C., &  
1438 Valdes, J. (2008). In situ measurement of mesopelagic particle sinking rates and the control of  
1439 carbon transfer to the ocean interior during the Vertical Flux in the Global Ocean (VERTIGO)  
1440 voyages in the North Pacific. *Deep Sea Research Part II: Topical Studies in Oceanography*,  
1441 55(14), 1684-1695. doi:10.1016/j.dsr2.2008.04.021
- 1442 Turner, J. T. (2002). Zooplankton fecal pellets, marine snow and sinking phytoplankton  
1443 blooms. *Aquatic microbial ecology*, 27(1), 57-102. doi:10.3354/ame027057
- 1444 Turner, J. T. (2015). Zooplankton fecal pellets, marine snow, phytodetritus and the ocean’s  
1445 biological pump. *Progress in Oceanography*, 130, 205-248. doi:10.1016/j.pocean.2014.08.005
- 1446 Volk, T., & Hoffert, M. I. (1985). Ocean carbon pumps: analysis of relative strengths and  
1447 efficiencies in ocean-driven atmospheric CO<sub>2</sub> changes. In E. T. Sundquist and W. S. Broecker  
1448 (Eds.), *The carbon cycle and atmospheric CO<sub>2</sub>: natural variations Archean to present* (Vol. 32,  
1449 pp. 99-110). Washington, D. C.: American Geophysical Union. doi:10.1029/GM032p0099

- 1450        Wang, W. L., Lee, C., & Primeau, F. W. (2019). A Bayesian statistical approach to inferring  
1451        particle dynamics from in-situ pump POC and chloropigment data from the Mediterranean Sea.  
1452        *Marine Chemistry*, 214, 103654. doi:10.1016/j.marchem.2019.04.006
- 1453        White, F. M. (1974). *Viscous fluid flow*. New York: McGraw-Hill Inc.
- 1454        Wilson, S. E., Ruhl, H. A., & Smith, J., K. L. (2013). Zooplankton fecal pellet flux in the  
1455        abyssal northeast Pacific: A 15 year time-series study. *Limnology and oceanography*, 58(3),  
1456        881-892. doi:10.4319/lo.2013.58.3.0881
- 1457        Woźniak, S. B., Stramski, D., Stramska, M., Reynolds, R. A., Wright, V. M., Miksic, E. Y., et  
1458        al. (2010). Optical variability of seawater in relation to particle concentration, composition, and  
1459        size distribution in the nearshore marine environment at Imperial Beach, California. *Journal of*  
1460        *Geophysical Research: Oceans*, 115(C8). doi:10.1029/2009jc005554
- 1461        Xiang, Y., & Lam, P. J. (2020). Size-fractionated compositions of marine suspended particles  
1462        in the Western Arctic Ocean: lateral and vertical sources. *Journal of Geophysical Research: Oceans*, 125(8), e2020JC016144. doi:10.1029/2020JC016144
- 1464        Xue, J., & Armstrong, R. A. (2009). An improved “benchmark” method for estimating  
1465        particle settling velocities from time-series sediment trap fluxes. *Deep Sea Research Part II: Topical Studies in Oceanography*, 56(18), 1479-1486. doi:10.1016/j.dsr2.2008.11.033
- 1467        Young, J. R. (1994). Functions of coccoliths. In A. Winter and W. G. Siesser (Eds.),  
1468        *Coccolithophores* (pp. 63-82). Cambridge, UK: Cambridge University Press.
- 1469